

# Tidal disruption event AT2020ocn: early-time X-ray flares caused by a possible disc alignment process

Z. Cao,<sup>1,2\*</sup> P.G. Jonker,<sup>2,1</sup> D.R. Pasham,<sup>3</sup> S. Wen,<sup>4,2</sup> N.C. Stone,<sup>5</sup> A.I. Zabludoff,<sup>6</sup>

<sup>1</sup>*SRON, Netherlands Institute for Space Research, Niels Bohrweg 4, 2333 CA Leiden, The Netherlands*

<sup>2</sup>*Department of Astrophysics/IMAPP, Radboud University, P.O. Box 9010, 6500 GL, Nijmegen, The Netherlands*

<sup>3</sup>*Kavli Institute for Astrophysics and Space Research, Massachusetts Institute of Technology, Cambridge, MA 02139, USA*

<sup>4</sup>*National Astronomical Observatories, Chinese Academy of Sciences, 20A Datun Road, Beijing 100101, China*

<sup>5</sup>*Racah Institute of Physics, The Hebrew University, Jerusalem, 91904, Israel*

<sup>6</sup>*Department of Astronomy and Steward Observatory, University of Arizona, 933 N. Cherry Ave., Tucson, AZ 85721, USA*

Accepted XXX. Received YYY; in original form ZZZ

## ABSTRACT

A tidal disruption event (TDE) may occur when a star is torn apart by the tidal force of a black hole (BH). Eventually, an accretion disc is thought to form out of stellar debris falling back towards the BH. If the star's orbital angular momentum vector prior to disruption is not aligned with the BH spin angular momentum vector, the disc will be tilted with respect to the BH equatorial plane. The disc will eventually be drawn into the BH equatorial plane due to a combination of the Bardeen–Peterson effect and internal torques. Here, we analyse the X-ray and UV observations of the TDE AT2020ocn obtained by *Swift*, *XMM-Newton*, and *NICER*. The X-ray light curve shows strong flares during the first  $\approx 100$  days, while, over the same period, the UV emission decays gradually. We find that the X-ray flares can be explained by a model that also explains the spectral evolution. This model includes a slim disc viewed under a variable inclination plus an inverse-Comptonisation component processing the slim disc emission. A scenario where the ongoing Lense–Thirring precession during the disc alignment process is responsible for the observed inclination variations is consistent with the data. In later observations, we find that the X-ray spectrum of AT2020ocn becomes harder, while the mass accretion rate remains at super-Eddington levels, suggesting the formation of a corona in line with accretion onto other compact objects. We constrain the BH mass to be  $(7_{-3}^{+13}) \times 10^5 M_{\odot}$  at the  $1\sigma$  (68%) confidence level.

**Key words:** X-ray astronomy – tidal disruption event – accretion physics

## 1 INTRODUCTION

A star can be broken apart by tidal forces when approaching a black hole (BH), triggering a tidal disruption event (TDE; e.g., Hills 1975; Rees 1988). A part of the stellar debris from the disrupted star will fall back towards the BH. The orbit of this fall-back material is expected to form an accretion disc (Rees 1988; Evans & Kochanek 1989; Ulmer 1999). Dozens of TDEs have been reported in the literature (Gezari 2021), and the number of candidates is increasing rapidly, thanks to large-scale sky surveys such as *Zwicky Transient Facility* (ZTF; Graham et al. 2019), *Asteroid Terrestrial-impact Last Alert System* (ATLAS; Tonry et al. 2018), and *All Sky Automated Survey for Supernovae* (ASAS-SN; Shappee et al. 2014).

The disruption often leads to processes that generate optical/UV and X-ray emission (e.g., Bade et al. 1996; Komossa et al. 2004; Gezari et al. 2006; van Velzen et al. 2011; Saxton et al. 2014; van Velzen et al. 2020; Saxton et al. 2020), which allows for the detection of massive BHs and the study of accretion processes. The thermal emission that is thought to originate in an accretion disc often dominates the TDE X-ray spectrum (e.g., Ulmer 1999; Lodato & Rossi 2011; Aucht et al. 2017). In some cases, non-thermal powerlaw-like X-ray emission is also observed (e.g., Saxton et al.

2017; Lin et al. 2017; Wevers et al. 2019b; Lin et al. 2020; Jonker et al. 2020). This non-thermal X-ray emission has been associated with the inverse-Comptonisation process where the thermal disc photons act as seed photons. While the late-time optical/UV emission (typically several hundred of days after the initial disruption) is consistent with originating from the disc (e.g., Van Velzen et al. 2019; Mummery & Balbus 2020; Wen et al. 2023), the origin of the early-time optical and UV emission is still a matter of debate (e.g., see Roth et al. 2020 for a review). One possibility is that UV photons are powered by the shocks (self-intersection shocks, or nozzle shocks) in the debris streams during the circularisation process, dissipating energy and angular momentum of the streams (e.g., Piran et al. 2015; Shiokawa et al. 2015; Ryu et al. 2020; Andalman et al. 2022; Steinberg & Stone 2022). Another possibility is that the UV emission comes from a "reprocessing layer" that captures the X-rays emitted by the inner disc and re-emits their energy in the UV (e.g., Loeb & Ulmer 1997; Metzger & Stone 2016a; Roth & Kasen 2018; Dai et al. 2018; Wevers et al. 2019b; Bonnerot & Lu 2020).

When the orbital angular momentum vector of the star prior to disruption is not aligned with the BH spin angular momentum vector, the disc plane might well be mis-aligned with respect to the BH equatorial plane (e.g., Stone & Loeb 2012; Franchini et al. 2016). Due to a combination of the Bardeen–Peterson effect (Stone & Loeb 2012) and internal torques (Franchini et al. 2016), (the inner part of)

\* E-mail: z.cao@srn.nl

this tilted disc will eventually be forced to align with the equatorial plane of a spinning BH. Predicted in theory and found in simulations, this disc alignment process manifests itself largely as Lense–Thirring precession, with the observed inclination angle of the disc varying during the process (e.g., [Fragile & Anninos 2005](#); [Franchini et al. 2016](#); [Zanazzi & Lai 2019](#); [White et al. 2019](#)). A varying disc inclination likely affects the broadband appearance of the source (e.g., [Dai et al. 2018](#)). It has been proposed that the disc alignment is important in explaining the highly–variable jet features observed in jetted TDEs (e.g., [Swift J164449.3+573451](#); [Tchekhovskoy et al. 2014](#); [Liska et al. 2018](#); see also [Teboul & Metzger 2023](#)).

TDE studies can help test accretion theories in the super–Eddington regime. The mass accretion rate in the disc formed after the disruption can vary from highly super–Eddington to sub–Eddington levels ([Strubbe & Quataert 2009](#); [Lodato & Rossi 2011](#); [Guillochon & Ramirez–Ruiz 2013](#); [Metzger & Stone 2016b](#)). In the high/super–Eddington regime, energy advection across the BH horizon can no longer be neglected, and the disc geometry is different from the standard Shakura–Sunyaev geometrically thin disc, instead the disc is geometrically thick ([Abramowicz et al. 1988](#)). In such cases, a "slim" disc model (e.g., [Abramowicz et al. 1988](#); [Sądowski 2009](#); [Sądowski et al. 2011](#)) is more appropriate than the standard thin disc model ([Shakura & Sunyaev 1973](#)). Furthermore, TDEs are good laboratories for studying the spectral evolution associated with the transition from super– to sub– Eddington mass accretion rate. Many TDEs show spectral state transitions in the X–rays along their decay (e.g., [Komossa et al. 2004](#); [Jonker et al. 2020](#); [Wevers et al. 2019b](#); [Cao et al. 2023](#)). Modelling the TDE X–ray spectrum allows to test whether such transitions appear under the same physical conditions as spectral state transitions observed in other super–Eddington accretors (e.g., ultra–luminous X–ray sources [ULXs]; [Gladstone et al. 2009](#); [Sutton et al. 2013](#); [Kaaret et al. 2017](#)).

The broadband source AT2020ocn (ZTF18aakelin) was first detected by ZTF in the optical on 2020–04–29 (Modified Julian Date, MJD 58968) and has been classified as a TDE candidate by [Gezari et al. \(2020\)](#). It is located at the centre of an otherwise quiescent, early type galaxy SDSS J135353.80+535949.7 at a redshift of  $z=0.0705$ . The  $M - \sigma_*$  relation suggests a BH mass of  $\sim 10^{6.4\pm 0.6}$  solar mass ([Pasham et al. 2024](#)). Subsequent observations by the *Neil Gehrels Swift* satellite revealed the source to be bright in the UV and the X–ray band ([Gezari et al. 2020](#); [Miller & Reynolds 2020](#)). *Neutron star Interior Composition Explorer (NICER)* started monitoring the source on 2020–07–11 (MJD 59041). Recently, [Pasham et al. \(2024\)](#) discovered a  $\sim 17$ –day quasi–periodicity modulating the X–ray flux of AT2020ocn as observed by *NICER* over the first  $\sim 130$  days. Various mechanisms can lead to this phenomenon, including a precessing accretion disc, as suggested by those authors. Therefore, spectral analysis with physical models is needed to see which mechanisms are consistent with the data.

In this paper, we use a standard  $\Lambda$ CDM cosmology with  $H_0 = 67.4$  km s $^{-1}$  Mpc $^{-1}$ ,  $\Omega_m = 0.315$  and  $\Omega_\Lambda = 1 - \Omega_m = 0.685$  ([Aghanim et al. 2020](#)) when converting the redshift to the luminosity distance. Throughout the paper,  $c$  is the speed of light,  $G$  is the gravitational constant,  $r$  is the radial coordinate measured from the BH centre, and  $R_g$  is the gravitational radius  $\frac{GM_\bullet}{c^2}$  for a BH of mass  $M_\bullet$ . We use  $R_*$  and  $M_*$ , for the stellar radius and mass of the star prior to the disruption, respectively.  $R_t$  is the tidal radius of the TDE, defined as  $R_t = R_*(M_\bullet/M_*)^{1/3}$ .

Here we analyse the light curves in the UV and X–ray bands, and spectra of AT2020ocn obtained by *Swift*, *XMM–Newton*, and *NICER*. The paper is structured as follows: In Section 2, we describe our data reduction method. In Section 3, we present the results from

our analyses. In Section 4 we discuss the physical scenarios implied by our modelling. In Section 5, we present our conclusions.

## 2 DATA AND DATA REDUCTION

### 2.1 NICER

We started our *NICER* data analysis with the raw/level–1 files available on the HEASARC public archive<sup>1</sup>. First, we reduced the data using the *nicerl2* task. Then, Good time intervals (GTIs) were produced with the default filters. We used the 3c50 background model ([Remillard et al. 2022](#)) to extract background spectra on a per GTI basis. Following the recommendations by [Remillard et al. \(2022\)](#) we excluded GTIs that do not pass the level–3 filtering. For more details of our procedure please see: [Pasham et al. \(2023, 2021\)](#). Both the background and the source+background spectra of *NICER* are rebinned by the optimal–binning algorithm ([Kaastra & Bleeker 2016](#); `ftool` command `ftgrouppha`). Also, we ensure that both the background and the source+background spectra have a minimum of 1 count per bin (with parameter `groupype` in `ftgrouppha` set to `optmin`).

Due to the super–soft X–ray nature of the source, *NICER* source counts are significantly below the background counts roughly above 1.1 keV for most of its observations. Therefore, we ignore *NICER* bands above 1.1 keV in this study. Meanwhile, to avoid spectra dominated by the noise in the background and uncertainties in estimating the background level, we exclude *NICER* observations where the source counts rate is lower than the background counts rate in 0.3–0.5 keV band. In this way, 1010 out of 1125 epochs of *NICER* observations remain.

When performing spectral analysis on *NICER* spectra, systematic errors of 1.5%<sup>2</sup> in the 0.3–1.1 keV band are added to the spectra using the "systematic" command in the XSPEC package ([Arnaud 1996](#); version 12.13.0c). We adjust the fitting energy range of each *NICER* spectrum using the `ignore` command in XSPEC, to discard the energy bins of the hard spectral tail where the source flux is lower than the background flux. The number of the discarded energy bins differs from epoch to epoch. Meanwhile, to have sufficient bins to fit a 2–parameter fit–function, we further require the spectrum to have a fitting energy range from 0.3 keV to at least 0.6 keV (>3 bins) to be considered for the fit procedure. In the analysis, data are considered to be consistent with the fit function if  $C\text{-stat}/d.o.f. < 2$ .

### 2.2 XMM–Newton

AT2020ocn was observed by *XMM–Newton* on three occasions during the *NICER* monitoring. The observations are identified by their ID: 0863650101 (XMM#1), 0863650201 (XMM#2), and 0872392901 (XMM#3). For the *XMM–Newton* data reduction, we use HEASOFT (version 6.31.1) and SAS (version 20.0.0) with the calibration files renewed on October 25th, 2022 (CCF release: XMM–CCF–REL–391). During XMM#2, the observation of two MOS detectors was interrupted for calibration purposes. Therefore, for consistency, we do not use the MOS data. We also do not use the RGS data, because the signal–to–noise ratio in the RGS detectors is too

<sup>1</sup> <https://heasarc.gsfc.nasa.gov>

<sup>2</sup> identical to the systematic errors applied by the *NICER* data reduction task `niphassyserr`. See [https://heasarc.gsfc.nasa.gov/docs/nicer/analysis\\_threads/spectrum-systematic-error/](https://heasarc.gsfc.nasa.gov/docs/nicer/analysis_threads/spectrum-systematic-error/)

**Table 1.** XMM-Newton observations of AT2020ocn analysed in this work. The exposure time is the time remaining after filtering for epochs of enhanced background count rates. The average count rates of the source+background spectra are given in the energy ranges 0.3–1.1 keV for XMM#1 & 2, and in 0.3–10.0 keV for XMM#3. We also list in the last column the source counts calculated by subtracting the estimated number of background counts in the source extraction region.

| Satellite  | ObsID (Label)      | Date       | Exposure (ks) | Source region       | Count rate (cts/s)              | Est. Source counts (cts) |
|------------|--------------------|------------|---------------|---------------------|---------------------------------|--------------------------|
| XMM-Newton | 0863650101 (XMM#1) | 2020-07-18 | 46            | annulus (15''-30'') | $(4.5 \pm 0.1) \times 10^{-2}$  | 1517                     |
|            | 0863650201 (XMM#2) | 2020-07-21 | 47            | annulus (15''-30'') | $(6.3 \pm 0.1) \times 10^{-2}$  | 2833                     |
|            | 0872392901 (XMM#3) | 2021-05-15 | 42            | circular (30'')     | $(67.6 \pm 0.4) \times 10^{-2}$ | 27546                    |

low. We use the SAS command `EPPROC` to process the Science 0 data from XMM-Newton/EPIC-pn. We employ the standard filtering criteria<sup>3</sup> for EPIC-pn data, where we require that the 10–12 keV detection rate of pattern 0 events is  $< 0.4$  counts  $s^{-1}$ . This way the data are cleared from periods with an enhanced background count rate. We use a circular source region of 30'' radius centred on the source for the spectral counts extraction, corresponding to a  $\sim 90\%$  energy fraction encirclement for a point source. Using the SAS command `EPATPLOT`, we check for the presence of photon pile-up, and find that XMM#1 and XMM#2 are suffered by pile-up while XMM#3 does not. To clean the spectra from the pile-up effect, we use an annulus region of 15'' inner radius and 30'' outer radius for the source counts extraction of XMM#1 and XMM#2. We find no pile-up effect in the data when using such an annulus source region. In all three XMM-Newton observations, the background spectral counts are extracted from apertures close to the source on the same EPIC-pn detector and free from other bright sources. We use a circular region of 50'' radius for the background extraction. Using the `specgroup` command in SAS, we re-bin both the background and the source+background spectra of XMM-Newton/EPIC-pn to have a minimum of 1 count per bin, while the oversampling factor is 3. We summarise the XMM-Newton data used in this paper in Table 1.

In this study we focus on the 0.3–10.0 keV band for the XMM-Newton/EPIC-pn data. We find in XMM#1 and XMM#2 the background counts dominate the source+background spectrum  $\geq 1$  keV. Therefore, we discard data above 1.1 keV during the analysis of XMM#1 and XMM#2, which is consistent with our treatment to the *NICER* data.

### 2.3 Swift

We complement our study of the X-ray flares of AT2020ocn with the UV data from the UVOT instrument (Roming et al. 2005) on-board *Swift* satellite. We reduce the archived *Swift*/UVOT images of AT2020ocn obtained between 2020-06-25 (MJD 59025) and 2021-06-22 (MJD 59387) using the `UVOTPRODUCT` task. We use a circular source region centred on the coordinates of AT2020ocn provided in the SIMBAD astronomy database<sup>4</sup>, using a standard radius of 5 arcsec as suggested by the *Swift* team<sup>5</sup>. We use an annulus centred on the source as the background region, with an inner radius of 10 arcsec and an outer radius of 25 arcsec. We also extract the soft X-ray light curve from the *Swift*/XRT instrument using the online XRT tool<sup>6</sup> (Evans et al. 2009), to compare with the X-ray behaviour of AT2020ocn as seen by *NICER*.

<sup>3</sup> <https://www.cosmos.esa.int/web/xmm-newton/sas-thread-epic-filterbackground>

<sup>4</sup> <http://simbad.u-strasbg.fr/simbad/>

<sup>5</sup> <https://www.swift.ac.uk/analysis/uvot/mag.php>

<sup>6</sup> [https://www.swift.ac.uk/user\\_objects/](https://www.swift.ac.uk/user_objects/)

Throughout this paper, we carry out the spectral analyses using the XSPEC package (Arnaud 1996; version 12.13.0c). We use Poisson statistics (Cash 1979; C-STAT in XSPEC). In this paper, we quote all the parameter errors at the  $1\sigma$  (68%) confidence level, assuming  $\Delta C\text{-stat}=1.0$  and  $\Delta C\text{-stat}=2.3$  for single- and two-parameter error estimates, respectively. In the figures the spectra are re-binned for plotting purposes only. In all fits we perform in this paper, we include the Galactic absorption using the model `TBabs` (Wilms et al. 2000), and we fix the column density  $N_{H,G}$  to its measured value at the host direction of  $1 \times 10^{20} \text{cm}^{-2}$  (Schlafly & Finkbeiner 2011). No intrinsic absorption is found by any of our fits in this paper. With the `energies` command in XSPEC, in all analysis we take a logarithmic energy array of 1000 steps from 0.1 to 1000.0 keV for model calculations instead of energy arrays from the response file, to be self-consistent and to correctly calculate the Comptonisation model when needed (see Section 3.3). When needed, we use the Akaike information criteria (AIC; Akaike 1974) to investigate the significance of adding model components to the fit-function, which is calculated by  $\Delta \text{AIC} = -\Delta C + 2\Delta k$  ( $C$  is the C-stat and  $k$  is the degree-of-freedom; Wen et al. 2018). The  $\Delta \text{AIC} > 5$  and  $> 10$  cases are considered a strong and very strong improvement, respectively, over the alternative model.

For each spectrum of XMM-Newton/EPIC-pn or *NICER*, we first fit the background spectrum with a phenomenological model. When fitting the source+background spectrum, we then add the best-fit background model to the fit function, fixing the parameters of the background model to their best-fit values determined from the fit to the background-only spectrum. The best-fit background model for XMM-Newton/EPIC-pn data varies from epoch to epoch, consisting of 1 Gaussian components and 2 power-law components for XMM#1 and XMM#2, or 3 power-law and 1 Gaussian components for XMM#3 that detects photons of higher energies, accounting for the background continuum and background fluorescence lines (e.g. Katayama et al. 2004). Meanwhile, we find the background spectra of *NICER* data can be described by a model consisting of 2 Gaussian components and 2 power-law components. The full-width half-maximum or FWHM  $\sigma_{\text{gauss}}$  is set to 0.001 keV for all the Gaussian components with a FWHM lower than the spectral resolution of XMM-Newton/EPIC-pn or *NICER*. In the following, when studying the source+background data, we refer only to the part of the fit function that describes the source as *fit function*.

## 3 RESULTS

### 3.1 Long-term light curve of AT2020ocn

We show the long-term UV and X-ray light curves of AT2020ocn in Fig. 1. Based on the *NICER* data, we find that the behaviour of the X-ray emission of AT2020ocn can be divided into two stages: an early period when strong X-ray flares are present (Modified Julian Date [MJD]  $\lesssim 59130$ ) and a late period of more gradual changes (MJD  $\geq 59130$ ). There are 375 epochs for the early period, and 635 for the late period. The *NICER* hard X-ray (0.85–1.1 keV) count

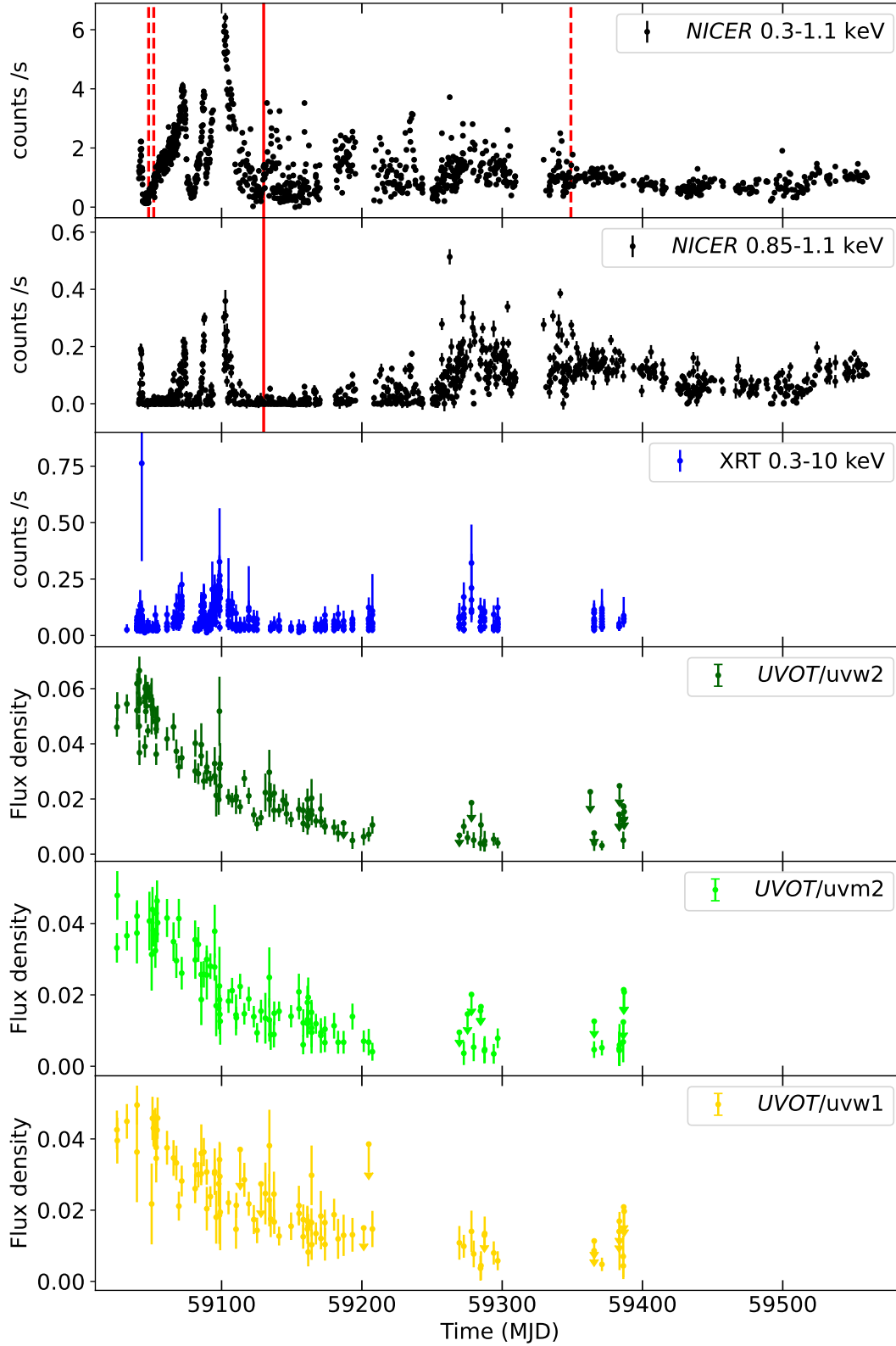


**Figure 1.** Long-term light curve of AT2020ocn as observed by *NICER* and *Swift*. From top to bottom: *NICER* count rate in the 0.3–1.1 keV band; *NICER* count rate in the 0.85–1.1 keV band; *Swift*/*XRT* count rate in the 0.3–10 keV band; the flux densities are in units of  $10^{-26}$  erg/s/cm<sup>2</sup>/Hz for the *Swift*/*UVOT* light curves in the uvw1, uvm2, and uvw2 filters. The x-axis denotes Modified Julian Date (MJD). Dashed lines in the top panel mark the times of the *XMM-Newton* observations (in this paper we refer to these as XMM#1, XMM#2, and XMM#3 in chronological order). The solid line marks MJD 59130, the date we use in this paper to separate the so-called early and late periods.

rate is low outside the flares in the early epoch data. The flares cannot be explained by background fluctuations (Fig. A1). In the late period, the light curve in the hard band shows a re-brightening around MJD 59300, with strong variations in the count rate. The X-ray light curve does not show a gradual decay in general. The *Swift*/XRT also detected the early X-ray flares. Meanwhile, the UV flux of AT2020ocn in all of the three UV bands of *Swift*/UVOT (uvw1, uvw2, and uvw3 band) decreases gradually with time, showing no evidence for flares such as those in the X-ray light curve. In other words, the X-ray and the UV light curves seem to be decoupled in the case of AT2020ocn.

### 3.2 Long-term spectral evolution of AT2020ocn

We study the spectral evolution of the source using the spectral hardness ratio in the *NICER* bands. We define the spectral hardness ratio as the ratio between the count rates in the 0.85–1.1 keV and the 0.3–0.5 keV bands. In analogy with the hardness–intensity diagram used often in X-ray binary studies, we present the hardness ratios of the *NICER* data of AT2020ocn as a function of the broadband count rate (0.3–1.1 keV) in Fig. 2. We find that the evolution of the hardness ratio is different for the early and the late period. Generally, during the early period the source spectrum is softer and the observed flux is higher. The hardness evolution during the 4 flares traces out a different region of the hardness–intensity diagram, showing a harder–when–brighter pattern within each flare. During the late period, the source hardness ratio is higher while the observed flux is lower.

We here use phenomenological model fits to the XMM-*Newton*/EPIC-pn spectra to investigate the spectral changes between the early and late spectra in some detail. Of the three XMM-*Newton* observations obtained during the *NICER* monitoring period (marked by dashed lines in Fig. 1), the observation XMM#1 and XMM#2 are in the early period while XMM#3 falls in the late period. We find that the XMM#1 and the XMM#2 spectra can be fitted well together (C-stat/d.o.f. = 20.5/31) with a fit–function comprised of two black body models (Fig. 3, we used the black body model `zbody` in XSPEC syntax). However, XMM#3 cannot be fitted well with such a fit function. Instead, it can be fitted with a power law with a photon index  $\Gamma = 2.89 \pm 0.01$  (C-stat/d.o.f. = 316.5/166). Fig. 3 shows the different XMM-*Newton*/EPIC-pn spectra. The XMM#3 spectrum is much harder than the other two spectra. This spectral difference between the early and late spectra observed by XMM-*Newton* is consistent with our findings based on the *NICER* data (Fig. 2).

### 3.3 Spectral analysis of X-ray data

#### 3.3.1 XMM#1 and XMM#2

To constrain parameters (such as the BH mass and spin, and the accretion rate) of AT2020ocn, we use the slim disc model `slimdz` (Wen et al. 2022) to simultaneously fit the two XMM#1 and XMM#2 spectra, allowing the mass accretion rate  $\dot{m}$  to vary between epochs. We find a good fit with the slim disc model (C-stat/d.o.f. = 26.4/34; XSPEC’s syntax “`TBabs*slimdz`”). As stated in Section 2, we fix the column density of the Galactic absorption ( $N_{H,G}$  in TBabs) to its measured value in the host’s direction  $1 \times 10^{20} \text{ cm}^{-2}$  (Schlafly & Finkbeiner 2011). We will keep using this  $N_{H,G}$  value and fix it during the fits for all the following fit–functions considered in this paper. For a  $1\sigma$ , single–parameter error estimate, the best–fit value for the BH mass  $M_\bullet$  is  $(7 \pm 1) \times 10^5 M_\odot$ , and for the inclination it is  $74^{+1}_{-11}$  degrees. The BH spin  $a_\bullet$  is constrained to have a lower limit of 0.25. We present the best–fit slim disc model in Fig. 4,

and the parameter constraints in Table 2. The accretion rate  $\dot{m}$  at these two epochs do not differ from each other by more than  $1\sigma$  error range. By investigating the  $\Delta$ C-stat across the  $\{M_\bullet, a_\bullet\}$  plane, we find a degeneracy between the BH mass and BH spin (Fig. 5): the lower limit on  $a_\bullet$  increases with increasing  $M_\bullet$ . In general,  $a_\bullet$  cannot be constrained. Specifically, the  $1\sigma$  lower limit on  $a_\bullet$  for a two–parameter error estimate, at the best–fit BH mass value, is  $a_\bullet > -0.1$ . We also find an equivalently–good fit with not  $\dot{m}$  but  $\theta$  varying between the two epochs (C-stat/d.o.f. = 26.1/34; Table 2). In this test case, the BH mass is  $M_\bullet = (7 \pm 1) \times 10^5 M_\odot$  and  $a_\bullet > 0.41$ ; the inclination  $\theta$  at these two epochs is consistent with being constant within  $1\sigma$  ( $74^{+1}_{-9}$  degree for XMM#1, and  $72^{+1}_{-9}$  degree for XMM#2).

#### 3.3.2 *NICER* spectra from the early flaring period

Given the results of the spectral fits to the XMM#1 and XMM#2 data, we try to fit the individual *NICER* spectra of the early flaring period using the same fit–function (TBabs\*`slimdz`). We aim to test whether allowing the values of one or more parameters of the slim accretion disc to vary can explain the spectral and flux variability observed by *NICER* over the early period. According to our selection criteria of *NICER* data as described in Section 2.1, a total of 206 epochs in the early period are considered for the spectral analysis. We list these epochs in Table A2.

For the slim disc fit function, we fix the BH mass  $M_\bullet$  to the best–fit value obtained from the joint XMM#1 and XMM#2 spectral fit using the same fit–function ( $7 \times 10^5 M_\odot$ ), and we fix the BH spin  $a_\bullet = 0.9$ . This spin value corresponds to the best–fit slim disc model to the joint XMM#1 & 2 spectra given our choice of the BH mass value (Fig. 5).

We first test whether the spectral evolution of the early period *NICER* data can be explained by a slim disc varying its accretion rate  $\dot{m}$  as well as its inclination angle  $\theta$  with respect to our line-of-sight. We find that for only 108 out of the 206 *NICER* early spectra this procedure gives a C-stat/d.o.f. < 2 (Fig. A2). The slim disc model fails to fit most of the spectra at the peak of each flare. Specifically, from the fit residuals we find the spectral hardening at the flare peaks makes the spectrum deviate from a slim disc model (e.g., Fig. A3). We conclude that the X-ray flares of AT2020ocn in the early period can not be fully explained by only varying the disc accretion rate  $\dot{m}$  and the inclination angle  $\theta$ .

A hard spectral component additional to a disc continuum in the X-ray spectra of BH accretion systems has been interpreted before to be due to inverse–Comptonisation (IC; e.g., Belloni 2010; Kubota & Done 2019; Mummery & Balbus 2021), where high–energy electrons scatter the soft disc photons to higher energies. This IC component is commonly used to explain the harder–than–disc BH spectra in many TDEs or ultra–luminous X-ray sources that have been proposed to be at near–/super–Eddington accretion rate (e.g., Magdziarz et al. 1998; Gladstone et al. 2009; Saxton et al. 2019; Wevers et al. 2021; Yao et al. 2022). Therefore, we test if the spectra at the peak of the flares can be fit well when including an IC component with seed photons coming from the slim disc, using the model `thcomp` (Zdziarski et al. 2020; the `thcomp` model parameterises the up–scattered spectra through the Thomson optical depth  $\tau$  and the electron temperature  $kT_e$ . The total fit function in XSPEC’s syntax is “`TBabs*thcomp*slimdz`”). We fix the covering fraction of `thcomp` to unity, so that all seed photons go through the Comptonising medium. Given the data quality we find parameter degeneracies in most epochs between the IC electron temperature  $kT_e$  and the IC optical depth  $\tau$ . The best–fit  $\tau$  is typically  $\geq 10$ . We therefore fix  $\tau = 20$  during the fit so that the IC component is parameterised by a single free parameter ( $kT_e$ ).

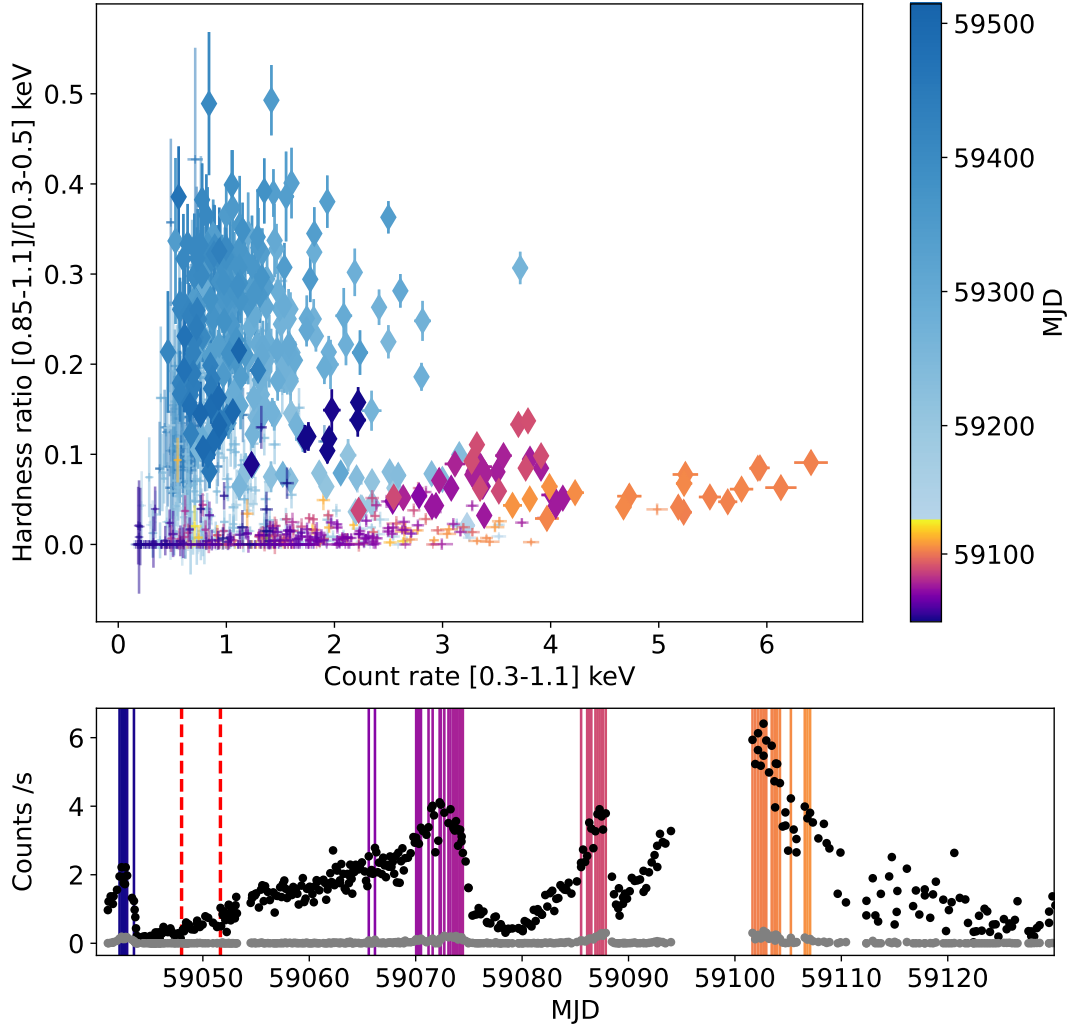


**Figure 2.** *Upper:* We show here the *NICER* hardness ratio vs. the *NICER* count rate in the 0.3–1.1 keV band. We define the spectral hardness ratio as the ratio between the count rate in the 0.85–1.1 keV band and that in the 0.3–0.5 keV band. The shown data are colour-coded by their observation time in MJD. We use different colours to show the hardness evolution during the early period (MJD < 59130; from purple to yellow), and during the late period (MJD > 59130; from light blue to dark blue). Epochs highlighted with diamond markers have the source count rate higher than the background count rate in the 0.85–1.1 keV band, so that their hardness ratios determined are least affected by the uncertainties in the *NICER* background estimation. *Bottom:* Zoom-in of the *NICER* early-time light curve (i.e., data obtained before 59130 MJD) also shown in the *top* panel in Fig 1. The black and grey data show the source count rates in the 0.3–1.1 keV and 0.85–1.1 keV band, respectively. The solid coloured vertical lines mark the observation times of the corresponding data highlighted by diamond markers in the upper panel, following the same colour scheme. From left to right, the red dashed lines mark the observation time of XMM#1 and XMM#2, respectively.

We find that for 165 out of the 206 *NICER* early spectra the fit procedure gives a C-stat/d.o.f. < 2 by assuming a similar  $\dot{m}$  as determined in XMM#1 & 2 ( $\dot{m} = 30 \dot{m}_{\text{Edd}}$ ). Each spectrum has at least 2 d.o.f. left to be fitted with a 2-parameter ( $\theta$  and  $kT_e$ ) fit function, and most of the not-well-fit spectra also give a C-stat/d.o.f. close to 2 (Fig. A4). We present the evolution of the parameter constraints produced from this fit procedure in Fig. 6. This slim disc+IC model can fit most of the spectra at flare peaks (e.g., Fig A5). We find that the Comptonising medium becomes hotter ( $kT_e \sim 0.3$  keV) during the flares, while the  $kT_e$  is lower ( $kT_e \lesssim 0.3$  keV) outside the flares. Meanwhile, no intrinsic absorption is needed to model any flares.

Next, we investigated if variations in  $\dot{m}$  and  $kT_e$  can explain the early X-ray flares instead of variations in  $\theta$  and  $kT_e$ . When fitting individual spectra, we fix  $\theta$  to the best-fit value determined from XMM#1 & 2 ( $74^\circ$ ) and let  $\dot{m}$  and  $kT_e$  free to vary. This fit procedure

results in a much lower number of spectra to be well-fit by the slim disc+IC model (59 spectra fitted instead of 165 for the procedure where  $\theta$  and  $kT_e$  are free to vary). Letting also  $\tau$  free to vary does not improve the fits. We conclude that the variation in inclination are likely to be important during the early period, while the  $\dot{m}$  variation is not the leading factor causing the flares.

### 3.3.3 The late-time spectrum observed in XMM#3

During the late-time period (MJD > 59130) XMM-Newton observed AT2020ocn once (XMM#3). The spectrum of XMM#3 can be well-fit by a power law with index  $\Gamma = 2.89 \pm 0.01$  (TBabs\*powerlaw; C-stat/d.o.f. = 316.5/166). However, there are trends in the residuals for this fit showing the model under-predicting the data systematically above 2 keV (Fig. 7). The fit can be then significantly

**Table 2.** Parameter constraints and the fit statistics from our joint-fits to the XMM#1 and XMM#2 spectra. Parameter values held fixed during the fit are given inside square brackets. In this table we quote the parameter errors derived using  $\Delta\text{C-stat}=1.0$  for single-parameter error estimates. The first joint-fit assumes a difference in the mass accretion rate  $\dot{m}$  between the two epochs, while the second joint-fit assumes a difference in the inclination  $\theta$ .

| Fit-function            | Epoch | Tbabs                         | slimdz                         |                 |                         |             |
|-------------------------|-------|-------------------------------|--------------------------------|-----------------|-------------------------|-------------|
|                         |       | $N_H/10^{20} \text{ cm}^{-2}$ | $\dot{m}/\dot{m}_{\text{Edd}}$ | $\theta/^\circ$ | $M_\bullet/M_\odot$     | $a_\bullet$ |
| Tbabs*slimdz            | XMM#1 | [1.0]                         | $> 17$                         | $74_{-11}^{+1}$ | $(7 \pm 1) \times 10^5$ | $> 0.25$    |
|                         | XMM#2 | =XMM#1                        | $19_{-6}^{+173}$               | =XMM#1          | =XMM#1                  | =XMM#1      |
| C-stat/d.o.f. = 26.4/34 |       |                               |                                |                 |                         |             |
| Fit-function            | Epoch | Tbabs                         | slimdz                         |                 |                         |             |
|                         |       | $N_H/10^{20} \text{ cm}^{-2}$ | $\dot{m}/\dot{m}_{\text{Edd}}$ | $\theta/^\circ$ | $M_\bullet/M_\odot$     | $a_\bullet$ |
| Tbabs*slimdz            | XMM#1 | [1.0]                         | $27_{-4}^{+171}$               | $74_{-9}^{+1}$  | $(7 \pm 1) \times 10^5$ | $> 0.41$    |
|                         | XMM#2 | =XMM#1                        | =XMM#1                         | $72_{-9}^{+1}$  | =XMM#1                  | =XMM#1      |
| C-stat/d.o.f. = 26.1/34 |       |                               |                                |                 |                         |             |

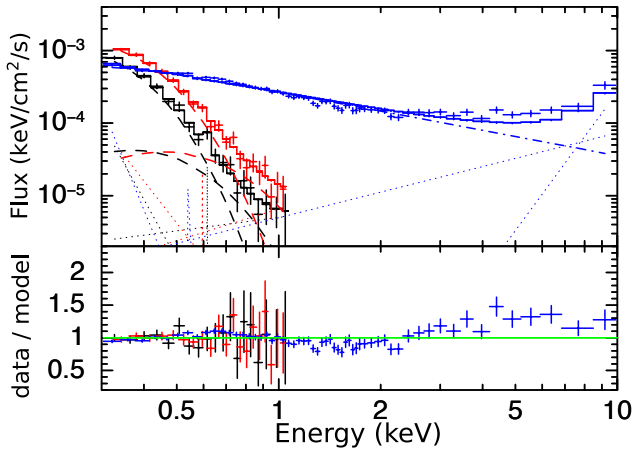


**Figure 3.** Top panel: We show the EPIC-pn source+background spectra of XMM#1 (black), XMM#2 (red), and XMM#3 (blue). The solid, dashed, dot-dashed and dotted lines represent the best-fit total models using phenomenological source models, the black body models used for XMM#1 & 2, the power-law model used for XMM#3, and the contribution from the background as determined from fitting extracted spectra from background-only data separately, respectively. The best-fit background power-law indices and Gaussian parameters have been held constant during the fit to the source+background spectra. Bottom panel: The ratio between the observed number of counts in each spectral bin (data; black, red and blue points in the top panel) and the best-fit predicted number of counts in each spectral bin (model; solid lines in the top panel) is shown.

improved using a fit-function consisting of a power law and a black body (C-stat/d.o.f. = 193.1/164 and  $\Delta\text{AIC} = 119.4$ ; XSPEC's syntax "TBabs\*(powerlaw+zbody)"). The black body model with a temperature of  $\sim 0.12$  keV accounts for part of the continuum at the soft end ( $< 2.0$  keV; Fig. A6).

Besides these phenomenological models, we use a fit-function to fit the spectrum of XMM#3 that contains TBabs\*thcomp\*slimdz. Like the case using a fit-function of a power-law, this fit-function does not describe the XMM#3 data well and has similar residuals. Part of the coronal emission can be reflected off the accretion disk, this reflection spectrum is calculated using the relxillCp model (Dauser et al. 2014; García et al. 2014). In relxillCp, the

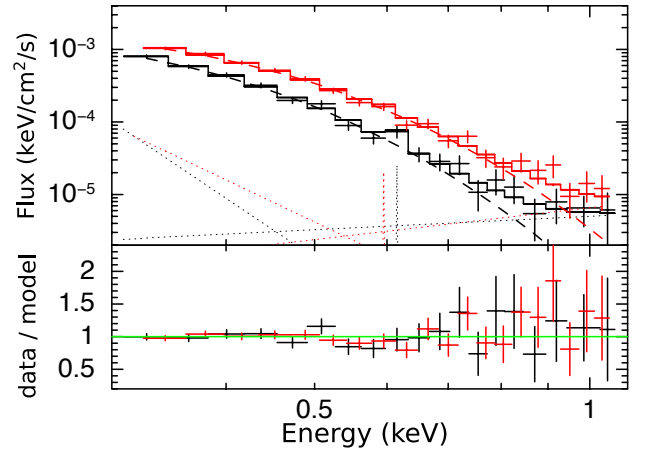


**Figure 4.** Top panel: the EPIC-pn XMM#1 (black) and XMM#2 (red) spectra of AT2020ocn fitted by a fit-function comprised of the following model components: TBabs\*slimdz. The solid, dashed, and dotted lines represent the best-fit total model, the slim disc emission, and the contribution from the background as determined from fitting extracted spectra from background-only data separately, respectively. The best-fit background power-law indices and Gaussian parameters have been held constant during the fit to the source+background spectra. Bottom panel: We show the ratio between the observed number of counts (data; red and black points in the top panel) and the best-fit predicted number of counts in each spectral bin (model; red and black solid lines in the top panel).

disc is assumed to be a standard Shakura–Sunyaev thin disc (Shakura & Sunyaev 1973), and the incident coronal emission is modelled by nthcomp (the now deprecated, stand-alone version of thcomp; Zdziarski et al. 1996, 2020), that assumes a multi-temperature black body seed spectrum. There are currently no reflection models using a slim disc for the disc seed photons, and so we use relxillCp to approximate the reflected emission off a slim disc. For this reason, one should be cautious when interpreting the results.

Overall, the total fit-function in XSPEC's syntax is "TBabs\*(thcomp\*slimdz+relxillCp)". Given the mentioned inconsistency of disc assumptions between the two model components, we do not try to measure the  $M_\bullet$  and  $a_\bullet$  values by analysing XMM#3 using this fit-function. Instead, we fix the

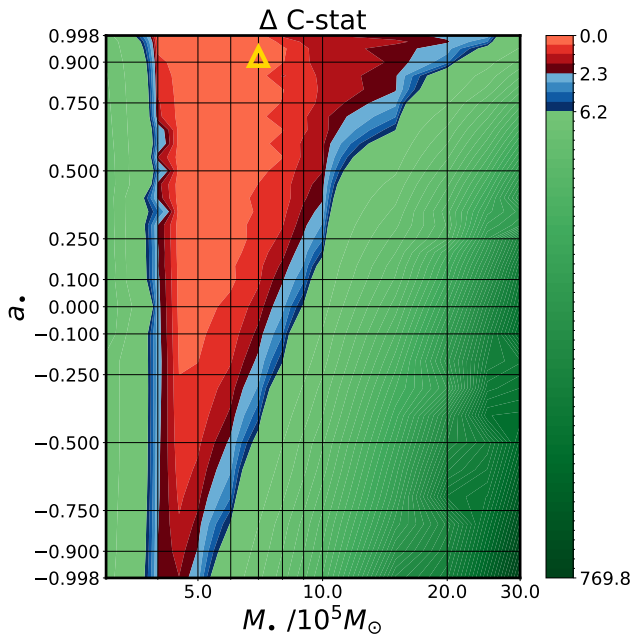


**Figure 5.** Constraints on  $M_*$  and  $a_*$  from the slim disc model-fit to the joint XMM#1 & 2 spectra. We calculate the  $\Delta$ C-stat across the  $\{M_*, a_*\}$  plane. The best-fit point with the lowest C-stat is marked by a yellow triangle. Areas within  $1\sigma$  and  $2\sigma$  for two-parameter error estimations are filled by red and blue colours, respectively. At  $1\sigma$  for the two-parameter fits,  $M_*$  is constrained to be  $(7^{+13}_{-3}) \times 10^5 M_\odot$ .

$M_*$  and  $a_*$  to their best-fit values from the analysis of XMM#1 & 2 (Fig. 5). The inclination  $\theta$  shared between the `slimdz` and `relxillCp` models is free to float in the fit but it is required to be the same between models. The  $kT_e$  shared between the `thcomp` and `relxillCp` models is also free to float in the fit but likewise it is required to be the same between models. We fix the  $\text{Refl}_{\text{frac}}$  parameter in `relxillCp` to be  $-1$  so that the model only accounts for the reflected emission. Other parameters for `relxillCp` that we have held fixed are: the iron abundance  $A_{\text{Fe}} = 1$  (in units of the solar abundance), the redshift  $z = 0.0705$ , the disc inner radius (ISCO;  $R_{\text{in}} = -1$  in `relxillCp`'s syntax), the disc's particle density  $\rho = 10^{17} \text{ cm}^{-3}$  from order-of-magnitude estimations (Stone 2015), and the disc outer radius  $R_{\text{out}} = 100R_g$  since that is the typical scale of a TDE disc for a BH of  $1 \times 10^6 M_\odot$  (Franchini et al. 2016; Zanazzi & Lai 2019). Since the X-ray emission is generated primarily in the inner-most accretion region, the disc outer radius will have little effect on the fit results. Finally, the reflection emissivity is set to be  $r^{-q}$  within  $15R_g$  and  $r^{-3}$  outside  $15R_g$  with  $q$  as a free parameter).

We find that the spectrum XMM#3 can be well-fit by such a fit-function (C-stat/d.o.f. = 175.0/159; Fig. 7). This fit statistic is better ( $\Delta\text{AIC} = 8.1$ ) than that of the phenomenological fit with a power law and a black body. Adding `relxillCp` into the fit-function improves the fit significantly ( $\Delta\text{AIC} = 96.8$ ) compared to the fit-function without the `relxillCp` model component ("`TBabs*(thcomp*slimdz)`"; C-stat/d.o.f. = 279.8/163). We find that the corona is optically thick ( $\tau \gtrsim 1$ ) and warm ( $kT_e < 10 \text{ keV}$ ), and the covering fraction of the corona over the disc continuum needs to be less than unity so that  $\sim 20\%$  of the disc photons are observed without being Comptonised. A full list of parameter constraints from the fit is presented in Table 3. Letting the disc's particle

**Table 3.** Best-fit parameter values obtained using a fit-function of `TBabs*(thcomp*slimdz+relxillCp)` to describe XMM#3's spectrum. Parameters held fixed, and their values are given in between square brackets. Parameter  $f_c$  is the covering fraction of the Comptonising medium. The unit of the normalisation of the `relxillCp` model is that of flux in the 0.3-10 keV band.

| Model     | Parameter                                  | Value                          |
|-----------|--|--------------------------------|
| TBabs     | $N_H / 10^{20} \text{ cm}^{-2}$            | [1.0]                          |
| thcomp    | $\tau$                                     | $8 \pm 3$                      |
|           | $kT_e / \text{keV}$                        | $2.4^{+1.4}_{-0.7}$            |
|           | $f_c$                                      | $0.8 \pm 0.1$                  |
| slimdz    | $\dot{m} / \dot{m}_{\text{Edd}}$           | $> 3.3$                        |
|           | $\theta / ^\circ$                          | $81^{+4}_{-7}$                 |
| relxillCp | $\Gamma$                                   | $1.5 \pm 0.2$                  |
|           | $q$  | $1.6 \pm 0.8$                  |
|           | $\log(\xi)$                                | $0.7 \pm 0.3$                  |
|           | $\text{Refl}_{\text{frac}}$                | [-1]                           |
|           | $\log(\rho / \text{cm}^{-3})$              | [17]                           |
|           | norm / $\text{erg cm}^{-2} \text{ s}^{-1}$ | $(1.3 \pm 0.3) \times 10^{-5}$ |
|           | C-stat/d.o.f.                              | 175.0/159                      |

density be a free parameter does not improve the goodness-of-fit ( $\Delta\text{AIC} = -0.1$ ), and neither does letting the iron abundance be a free parameter ( $\Delta\text{AIC} = -2$ ).

### 3.4 Analysis of UV data using MOSFiT

We analyse *Swift*/UVOT photometry data for the observations listed in Table A1 using the Modular Open Source Fitter for Transients (MOSFiT; Guillochon et al. 2018). The assumptions and details of its TDE module can be found in Mockler et al. (2019). In summary, the module simultaneously fits the UV light curves using a library for model light curves derived using hydrodynamical simulations of TDEs (Guillochon & Ramirez-Ruiz 2013). The fallback mass rate  $\dot{M}_{\text{fb}}(t)$  as a function of time is determined from the simulations by varying the  $M_*$ , the stellar mass  $M_*$ , and the scaled impact parameter  $b^7$ . Then the  $\dot{M}_{\text{fb}}$  is transformed into a viscously-delayed accretion rate  $\dot{M}_{\text{acc}}$  using the viscous timescale  $T_{\text{visc}}$  (eq. 7 in Mockler et al. 2019). The module assumes a time-independent efficiency  $\epsilon$  in the energy conversion from  $\dot{M}_{\text{acc}}c^2$  to a bolometric luminosity  $L$  so that  $L = \epsilon\dot{M}_{\text{acc}}c^2$ . Then assuming thermal radiation, this radiation is emitted from a photosphere with an effective temperature  $T_{\text{eff}}(L, R_{\text{ph}})$ , where the photospheric radius  $R_{\text{ph}} = R_{\text{ph},0}a_p(L/L_{\text{Edd}})^{l_{\text{ph}}}$ . Here  $R_{\text{ph},0}$  is a normalising factor, and  $l_{\text{ph}}$  is an exponential index (eq. 9& 10 in Mockler et al. 2019). The  $a_p$  can be regarded as the semimajor axis of the averaged bound orbit of material being accreted when the  $\dot{M}_{\text{fb}}$  is at its peak.

The fit parameters are  $M_*$ ,  $M_*$ ,  $b$ ,  $T_{\text{visc}}$ ,  $\epsilon$ ,  $R_{\text{ph},0}$ ,  $l_{\text{ph}}$ , the difference

<sup>7</sup> The impact parameter  $\beta$  can be calculated from  $b$ : if  $0 \leq b < 1$ ,  $\beta = 0.6 + 1.25b$  when  $\gamma = 4/3$ , and  $\beta = 0.5 + 0.4b$  when  $\gamma = 5/3$ ; if  $1 \leq b \leq 2$ ,  $\beta = 1.85 + 2.15(b - 1)$  when  $\gamma = 4/3$ , and  $\beta = 0.9 + 1.6(b - 1)$  when  $\gamma = 5/3$ . Here  $\gamma$  is the polytropic index of the disrupted star so that the equation-of-state of the star is  $P \propto \rho^\gamma$  ( $P$  is the pressure and  $\rho$  is the density). See more in Guillochon & Ramirez-Ruiz 2013 and Mockler et al. 2019.



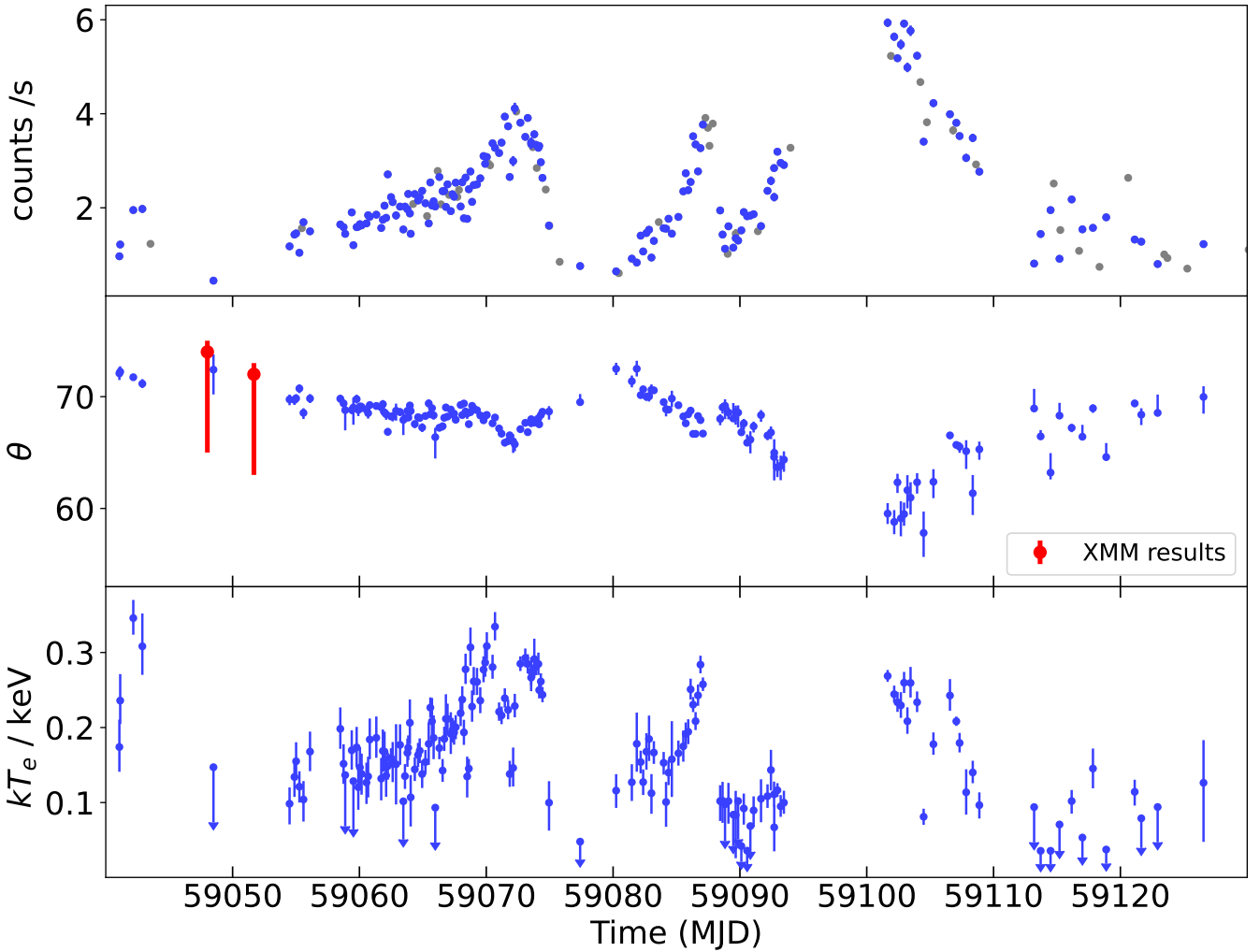


**Figure 6.** *Top panel:* The *NICER* 0.3–1.1 keV early-time source light curve. We only consider the epochs where the source flux stays above the background level from 0.3 keV to at least 0.6 keV (a total of 206 epochs in the early period). Spectra at epochs marked by blue dots are well-fit ( $C\text{-stat}/d.o.f. < 2$ ) by the model in this analysis, while grey dots mark spectra that have  $C\text{-stat}/d.o.f. > 2$ . *Middle panel:* Inclination  $\theta$  constraints derived from the *NICER* spectra obtained before MJD 59130. The fit-function is comprised of the following model components: `TBabs*(thcomp*slimdz)`. We fit each of the 206 spectra individually allowing the inclination  $\theta$ , and the temperature of the Comptonising medium  $kT_e$  to vary. We fix  $M_\bullet = 7 \times 10^5 M_\odot$  and  $a_\bullet = 0.9$  based on the results of the spectral fits to the *XMM-Newton* data (Fig. 5). The slim disc accretion rate  $\dot{m}$  and the optical depth of the Comptonising medium are held fixed at a value of  $30 \dot{m}_{\text{Edd}}$  and  $\tau = 20$ , respectively. We show the fit parameter values for the 165 out of the 206 spectra where the  $C\text{-stat}/d.o.f. < 2$  (the results from the blue points in the top panel). The inclinations constrained from the joint-fit to the XMM#1 and XMM#2 X-ray spectra are marked with the red dots. *Bottom panel:* Constraints on the electron temperature  $kT_e$  derived from the same fitting procedure described above.

$t_0$  between the time at peak luminosity and the time of the first detection, and the host column density  $N_{\text{H,host}}$ . Given no intrinsic absorption is found in the X-ray analysis, we fix the  $N_{\text{H,host}} = 1 \times 10^{19} \text{ cm}^{-2}$  an order-of-magnitude lower than the Galactic column density in the host direction. No other parameter values are fixed. We use the Markov–Chain–Monte–Carlo (MCMC) routine in MOSFIT to perform the fit. We set 20 walkers and run for 30,000 iterations. We then exclude the first 10,000 iterations as burn-in. In MOSFIT, the goodness-of-fit and the chain convergence are measured using the Watanabe–Akaike information criteria (WAIC; Watanabe & Opper 2010) and the potential scale reduction factor (PSRF; Gelman & Rubin 1992), where a fit with  $\text{PSRF} \leq 1.2$  is considered to have converged.

We find the MOSFIT produces a fit to the data with  $\text{PSRF}=1.167$

and  $\text{WAIC}=207$ . A full list of the parameter values and their uncertainties is presented in Table 4. We find the  $M_\bullet$  is constrained to be between  $5 \times 10^5$  and  $5 \times 10^6 M_\odot$ , which is in agreement with our black hole mass measurement using spectral fits to the X-ray data. The systematic errors for each fitting parameter estimated from Mockler et al. (2019) are also given in Table 4. We note for parameters other than  $M_\bullet$ , the systematic errors are large compared to the  $1\sigma$  error range given by the fitting procedure. This conclusion also holds if we treat the  $M_\bullet$  as a known value taken from the analysis of X-ray data (Fig. 5) when performing the fit. We present the data as well as the best-fit MOSFIT model in Fig. A7.

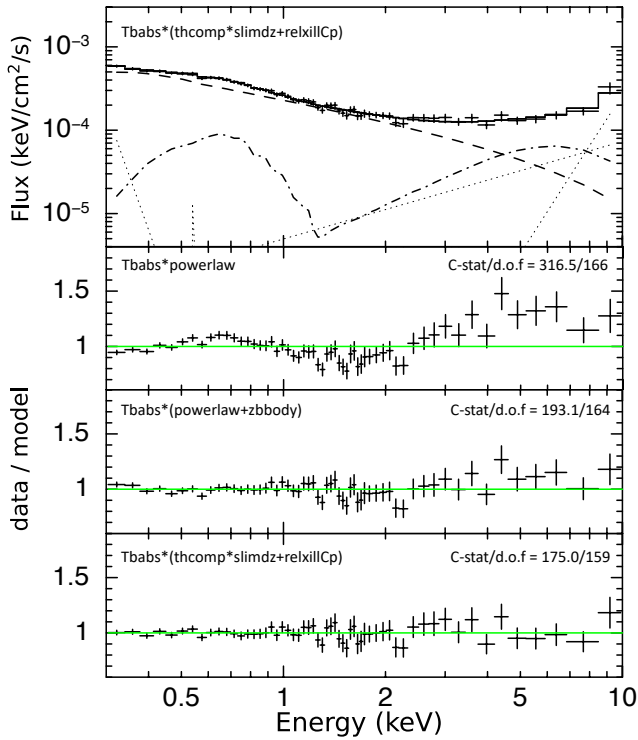


**Figure 7.** *Top panel:* The X-ray spectrum and the best-fit "TBabs\*(thcomp\*slimdz+relxillCp) model for the XMM#3 observation. The solid, dashed, and dot-dashed lines represent the best-fit total model, the coronal component thcomp\*slimdz, and the corona reflection relxillCp, respectively. The dotted black lines show the contribution from the background as determined from fitting separately background-only spectra. The best-fit background power-law indices have been held constant during the fits to the source spectrum. *Upper-middle panel:* The ratio between the observed number of counts (data) and the best-fit predicted number of counts in each spectral bin (model), for a source fit-function of "TBabs\*powerlaw" to describe the XMM#3 spectrum. *Lower-middle panel:* The ratio between the data and the model for a source fit-function of "TBabs\*(powerlaw+zbody)" to describe the XMM#3 spectrum. *Bottom panel:* The ratio between the data and the model for the source fit-function of "TBabs\*(thcomp\*slimdz+relxillCp)" shown in the top panel.

**Table 4.** Parameters and their constraints derived from modelling the *Swift*/UVOT light curves using MOSFIT. See the text for the meaning of each parameter. Systematic errors are taken from Mockler et al. (2019).

| Parameter                             | Value            | Systematic Error |
|---------------------------------------|------------------|------------------|
| $\log(M_{\bullet} / M_{\odot})$       | $6.2 \pm 0.3$    | $\pm 0.2$        |
| $\log(M_{*} / M_{\odot})$             | $-0.01 \pm 0.09$ | $\pm 0.66$       |
| $b$                                   | $1.2 \pm 0.2$    | $\pm 0.35$       |
| $\log(T_{\text{visc}} / \text{days})$ | $< 0.6$          | $\pm 0.1$        |
| $\log(\epsilon)$                      | $-3.4 \pm 0.1$   | $\pm 0.68$       |
| $\log(R_{\text{ph},0})$               | $-0.4 \pm 0.3$   | $\pm 0.4$        |
| $l_{\text{ph}}$                       | $0.05 \pm 0.04$  | $\pm 0.2$        |
| $t_0 / \text{days}$                   | $-19 \pm 6$      | $\pm 15$         |

## 4 DISCUSSION

In this paper we present XMM-Newton/EPIC-pn and NICER X-ray spectral analysis of AT2020ocn. The X-ray data can be divided into two periods: an early period with flares (MJD  $\leq 59130$ ), and a late period without flares. Over the same period, the UV light curves observed by *Swift* show a gradual decay (Fig. 1). No evidence for UV flares is found.

We show that the spectra in the early period can be well-fit by a slim disc (Wen et al. 2020, 2022) plus an inverse-Comptonisation (IC) model (Zdziarski et al. 2020). Specifically, the spectral evolution along the flares can be explained by variations in the disc inclination and the electron temperature  $kT_e$  of the Comptonising medium. Using this fit-function, we constrain the BH mass to be  $(7^{+13}_{-3}) \times 10^5 M_{\odot}$ , while there is no constraint on the BH spin. The best-fit BH mass derived from analysing the UV data with the TDE module of MOSFIT is consistent with this result. Using the empirical  $M - \sigma_{*}$  relation and a velocity dispersion of the stellar absorption lines  $\sigma_{*} = 82 \pm 4$  km/s, Pasham et al. (2024) estimate the BH mass to be  $\sim 10^{6.4 \pm 0.6} M_{\odot}$ . The consistency between different methods further prove that AT2020ocn can be explained as a tidal disruption of a star by a massive BH.

The observed inclination variation along the flares can be caused by Lense-Thirring precession during the disc alignment process (e.g., Stone & Loeb 2012; Franchini et al. 2016). Such inclination variations have been observed in simulations (e.g., Fragile & Anninos 2005; Zanazzi & Lai 2019; White et al. 2019), and they have been proposed to explain the highly-variable jet features in jetted TDEs (e.g., Swift J164449.3+573451; Tchekhovskoy et al. 2014; Liska et al. 2018; see also Teboul & Metzger 2023). For a fast-spinning BH of  $M_{\bullet} = 10^6 M_{\odot}$ , the Lense-Thirring precession period during the disc alignment process is calculated to be  $\sim 10$  days (Franchini et al. 2016; Zanazzi & Lai 2019), and the timescale for the whole alignment phase is  $\leq 10^2$  days (Franchini et al. 2016). Such timescales for AT2020ocn are in agreement with the calculations (a duration of  $\sim 1 - 10$  days for individual flares, and the source stops flaring  $\leq 200$  days after the first *Swift* detection of the event). Pasham et al. (2024) discovered a  $17.0^{+1.2}_{-2.4}$ -day quasi-periodicity in NICER data in the early-time period, using an energy band of 0.3–1.0 keV that is slightly different from that in our study (0.3–1.1 keV). Without assuming their best-fit period, we fit the early-time NICER spectra and find an evolution of the  $\theta$  and the IC strength. We investigated if the already-found periodicity in the light curve data (Pasham et al. 2024) can also be found in a Lomb-Scargle periodogram (LSP; Lomb 1976; Scargle 1982) of our best-fit  $\theta$  or  $kT_e$  parameter values as a function of time. An LSP is designed to search for (quasi-)periodic signals in unevenly-sampled time series. In the frequency domain, we find that LSPs of the count rate in 0.3–1.1 keV and the  $kT_e$  as a function of time show periodicity peaks that are consistent with those found in Pasham et al. (2024), while the LSP of the  $\theta$  as a function of time only shows peaks at  $\leq 3\sigma$  significance level assuming a white-noise background (Fig. A8). It is possible that, as the IC component dominates the spectrum when the inclination decreases, most of the periodicity is imprinted in the IC component while the periodicity in  $\theta$  is less pronounced. A thorough timing analysis of the NICER early-time data, where the impact of the background red-noise is included in estimating the detection significance, can be found in Pasham et al. (2024).

The electron temperature  $kT_e$  of the IC component traces the spectral hardness ratio (Left panel Fig. 8): for all flares a higher  $kT_e$  is found when the spectrum becomes harder. This correlation is expected: the higher the temperature, the more energy a single photon

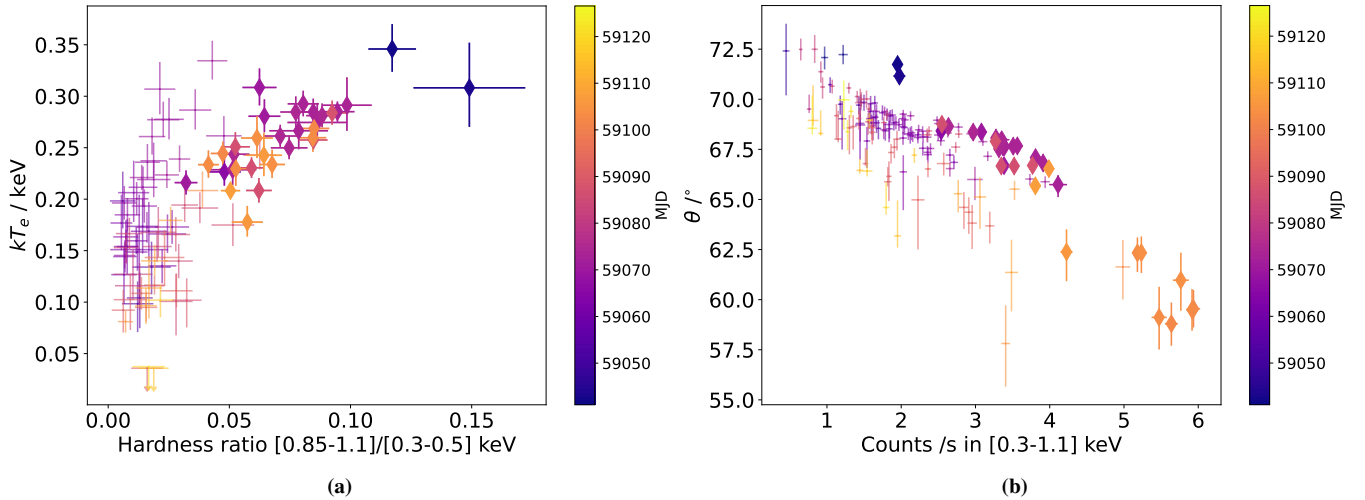


**Figure 8.** *Left panel:* The electron temperature  $kT_e$  vs. spectral hardness ratio, derived from the fit procedure producing Fig. 6. The epochs are colour-coded by their observation time in MJD. Epochs highlighted with diamond markers have a source count rate higher than the background count rate in the 0.85–1.1 keV energy band, so their hardness ratios are least affected by uncertainties in the *NICER* background estimation. The hardness ratio is traced by the temperature  $kT_e$  for all flares. *Right panel:* The disc inclination  $\theta$  vs. the total count rate in the 0.3–1.1 keV energy band. Generally, the lower the  $\theta$ , the higher the count rate in the 0.3–1.1 keV band. The spectra at the X-ray flare peaks are hard, which can be explained by enhanced inverse-Comptonisation. Some disc photons with energies  $< 0.3$  keV are up-scattered into the 0.3–1.1 keV band, more than those being scattered out, resulting in a higher count rate than that predicted by a model including only a slim disc.

is likely to get from the up-scattering events before escaping the Comptonising medium, thus the harder the emergent photon spectrum. A possible supply of high-energy electrons for the IC process comes from a disc outflow. For sources at high/super-Eddington accretion rates, a disc outflow is seen in both simulations (e.g., Ohsuga & Mineshige 2011; Takeuchi et al. 2013; Kitaki et al. 2021) and observations (e.g., Middleton et al. 2013; Pinto et al. 2016; Kara et al. 2018; Pinto et al. 2021). However, for AT2020ocn, the lack of high-resolution X-ray spectral data with a sufficient signal-to-noise ratio (e.g., from XMM-Newton RGS) precludes confirmation of the presence of a disc outflow.

In addition, we find an inverse correlation between  $\theta$  and the count rate in 0.3–1.1 keV band (*Right panel* in Fig. 8). This behaviour can be understood as follows: as the inclination decreases, more photons from the inner disc region are observed. The slim disc model predicts a harder and brighter disc continuum the more the inner disc region is observable (e.g., Wen et al. 2020, 2022). As the source flux increases along each flare, we detect the IC component. Some disc photons with energies  $< 0.3$  keV are up-scattered into the 0.3–1.1 keV band by the Comptonising medium, more than those being scattered out of this energy band, resulting in a higher count rate than that predicted by only a slim disc. We find that the inverse-Comptonisation starts to be detected at higher inclinations along the first flare compared to the subsequent flares, distinguishing the first flare from the rest in both the hardness ratio vs. count rate diagram (Fig. 2 and Fig. 8).

A physical link between the strengthening/weakening of the IC component, and the inclination variation of the disc, is possible, as indicated by the analysis of the early-time *NICER* data. Simulations suggest that when a massive BH accretes at super-Eddington levels, in the scenario of a powerful disc outflow, the temperature of the inner accretion region reaches  $\gtrsim 10^6$  K (corresponding to  $\gtrsim 0.09$  keV; e.g., Jiang et al. 2019; Yang et al. 2023). Our results are consistent with the picture that, as the disc inclination decreases, more photons from the hotter accretion region at smaller radii are observed. Thus, we

observe the temperature  $kT_e$  of electrons participating the IC process to increase during the X-ray flares, and its value ( $\sim 0.3$  keV) is similar to the value expected from simulations.

In our analysis, for the *NICER* spectra that are not well-fit by the slim disc+IC model, residuals may be caused by any or several of the following reasons: 1) The background in the source+background spectrum deviates from the background spectrum generated from *NICER* prescriptions. 2) The source spectrum varies during the exposure of a single epoch (typically  $\sim$ ks). The slim disc model assumes a steady-state. Given a slim disc of  $M_\bullet = 7 \times 10^5 M_\odot$ ,  $a_\bullet = 0.9$ , and  $\dot{m} = 30\dot{m}_{\text{Edd}}$ , the disc viscous timescale  $t_{\text{vis}} = \alpha^{-1}\Omega^{-1}(R)(H/R)^{-2}$  in the inner disc region (e.g.,  $\lesssim 10 R_g$ ) is  $\sim$  ks. Here  $\alpha$  is the Shakura-Sunyaev viscosity parameter (Shakura & Sunyaev 1973),  $H(R)$  is the disc height, and  $\Omega(R)$  is the orbital frequency; with such a high  $\dot{m}$ , the scaled disc height  $H/R$  reaches  $\sim 0.4$  at  $10 R_g$ . The photons from the inner disc region dominate the disc spectrum. Thus, on a timescale similar to the exposure time of individual *NICER* epochs, the steady-state approximation of the slim disc model may not be 100% valid. 3) Meanwhile, other physical mechanisms such as disc outflow (e.g., Middleton et al. 2013; Kara et al. 2018), or disc reflection (e.g., Masterson et al. 2022) could affect the observed TDE spectrum. With the current data, it is not possible to disentangle different origins of the residuals. Given that most of the early-time *NICER* spectra are describe well by our fit-function, we conclude that a slim disc+IC model describes the source X-ray spectrum well, and the observed long-term ( $\gtrsim 10$  days) variation of the disc inclination is not due to variations in the physics of the disc.

We test if the enhancement of the IC component during the flares can be explained by an increase in the covering fraction or the optical depth  $\tau$  of the Comptonising medium, instead of an increase in  $kT_e$ . We find that a slim disc plus a Comptonising medium with a varying covering fraction (with fixed  $kT_e = 0.3$  keV and  $\tau = 20$ ) can describe 140 out of 206 early-time *NICER* spectra (C-stat/d.o.f.  $< 2$ ). The value of the covering fraction in a black hole accretion system has

sometimes be found to be  $\lesssim 0.5$  (e.g., [Done & Kubota 2006](#); [Wilkins & Gallo 2015](#); [Chen et al. 2022](#); [Dai et al. 2023](#)), while in other cases it is consistent with the maximum value of 1 (e.g., [Tripathi & Dewangan 2022](#); [Liu et al. 2023](#); [Cao et al. 2023](#)). We re-run the fitting procedure as used for Fig. 6 but fixing the covering fraction to 0.5 instead of 1. In this case, we find that 152 out of 206 spectra are well-fit (Fig. A9), and both the  $\theta$  and  $kT_e$  behaviour is similar to Fig. 6. Similarly, a slim disc plus a Comptonising medium with a varying optical depth (with fixed  $kT_e = 0.3$  keV and a covering fraction of unity) can describe 153 spectra. It is possible that during each flare multiple parameters of the Comptonising medium are varying as the disc inclination changes. However, with the current data, it is not possible to disentangle the effects of different IC parameters. Nonetheless, in all the tests, the IC becomes prominent at different  $\theta$  values between the first and the subsequent flares (e.g., Fig. 8). Our tests on the IC parameters suggest that the physical properties of the Comptonising medium vary between flares.

Given the large uncertainties in constraining the BH spin from the XMM-Newton data (Fig. 5), we test if our findings about the  $\theta$  and  $kT_e$  behaviour are sensitive to the choice of  $a_\bullet$ . We perform the fit procedure described in Section 3.3.2, but with fixed  $M_\bullet = 5 \times 10^5 M_\odot$  and  $a_\bullet = 0.2$ . We find that 160 spectra are well-fit (Fig. A10). The variation behaviour of both  $\theta$  and  $kT_e$  is qualitatively similar to that in Fig. 6, but the range over which the inclination varies is much larger for the  $a_\bullet = 0.2$  case (the smallest inclination value within the concerned period from  $\sim 57^\circ$  to near-zero). This enlarged variation is to be expected: for  $a_\bullet = 0.2$  the inner edge of the disc is further away from the BH yielding a lower temperature and subsequently, a softer spectrum, as the innermost-stable-circular-orbit (ISCO) lies further away from the BH event horizon (the inner edge of the disc is set to the ISCO in the `slimdz`). As the inclination decreases, more hard ( $> 1$  keV) photons from the inner disc are observed, explaining the flares. Therefore, to get the same increase in flux of hard X-ray photons, the inclination must reach a value closer to zero for  $a_\bullet = 0.2$ , compared to the situation for  $a_\bullet = 0.9$ . Meanwhile, the peak features in  $\theta(t)$  with respect to time  $t$  occur at similar  $t$  for both cases. We conclude that, qualitatively, our findings about the  $\theta$  and  $kT_e$  behaviour with respect to time are not sensitive to the choice of BH spin during the *NICER* fitting procedure.

We also test if the early-time AT2020ocn data can be equally-well described by a slim disc plus a blackbody component instead of an IC component. We perform the fitting procedure similar to that producing Fig. 6, but replacing the IC model `thcomp` by a blackbody model `zbbody`. The XSPEC's syntax for the test fit-function is then `TBabs*(zbbody+slimdz)`. We find a large fraction of the *NICER* spectra cannot be well-fitted with a varying black body of  $kT_e \sim 0.3$  keV (Fig. A11; only 71 out of 206 have a C-stat/d.o.f.  $< 2$ ). Allowing the black body temperature to be free-to-vary during the fitting procedure increases the number of good fits to 115 out of 206 but this is still less than in the number of good fits when using the slim disk plus IC component (see Fig. 6; 165 out of 206 fits are good, with one more d.o.f. than the case of `zbbody` in each individual fit). Therefore, we conclude that a variable IC component provides a better description of the data compared to a varying black body component. To summarise the different fits and tests we perform for the early-time *NICER* data, we list them in Table 5. For reference, we also show the histograms of C-stat/d.o.f. for each fit in Fig. A12.

We note there are several limitations to our modelling. One key assumption in the `slimdz` model is that the disc is aligned with the BH equatorial plane. In this paper we find that the early-time X-ray flares are well-explained by a variable inclination, and we interpret it as results from the disc alignment process. We are not

modelling the dynamic solutions of a precessing disc, and there are currently no analytic solutions of a tilted slim disc (i.e., with the disc outside the equatorial plane). Changing  $\theta$  in the model is really changing the observer's direction, which is not identical to a precessing disc while the observer is on a fixed position regarding the Kerr metric. Therefore, it is important that we try to estimate the deviations of a disc described by the `slimdz` model from a tilted disc. From Fig. 6 we find the amplitude of the inclination variation to be  $\lesssim 10^\circ$ . In such a case, we estimate a change of  $1 - \sin^2(90^\circ - 10^\circ) \approx 3\%$  in the tilted disk metric from the approximate equatorial metric of a Kerr black hole, corresponding to a change of 3% in the estimation of accretion rate ([Page & Thorne 1974](#)). Furthermore, using general relativistic magnetohydrodynamic simulations, [Fragile et al. \(2007\)](#) find that the tilt will change the inner radius of the disc, consequently impacting the efficiency of disk radiation. By studying the disc properties, they conclude that effectively, a tilted disc acts like an un-tilted disc with a lower black hole spin. In this sense, we estimate the tilt-induced X-ray flux change by comparing two slim discs with the same accretion rate but different spin values. Assuming  $M_\bullet = 7 \times 10^5 M_\odot$ ,  $\dot{m} = 30 \dot{m}_{\text{Edd}}$ , and  $\theta = 60$ , we estimate the flux difference between an un-tilted slim disc with  $a_\bullet = 0.998$ , and a 10-degree-tilted disc approximated by a disc with  $a_\bullet = 0.998 \sin(90^\circ - 10^\circ) = 0.983$ , to be  $\sim 10\%$  (from  $\sim 5.13 \times 10^{-12}$  erg cm $^{-2}$  s $^{-1}$  to  $\sim 4.67 \times 10^{-12}$  erg cm $^{-2}$  s $^{-1}$ ) in the energy range 0.3-1.5 keV. The full impact of tilt on the disc physics necessitates further investigation, which is beyond the scope of this paper.

Meanwhile, parameter constraints ( $M_\bullet, a_\bullet, \text{etc.}$ ) from the `slimdz` might be impacted by this tilt nature of the disc. We estimate the parameter deviations by comparing the results from the early-time spectra with those from the late-time spectra. XMM#3 is taken after the flaring period, likely when the disc has settled in the equatorial plane. We re-fit the XMM#3 spectrum with the model in Table 3 but let also  $M_\bullet$  and  $a_\bullet$  free-to-vary (though note the consistency issue between `thcomp` and `relxillCp`). In this test we find a C-stat/d.o.f. of 174.4/157 ( $\Delta\text{AIC} = -3.4$ , meaning the improvement of including an additional free parameter is not significant). The BH mass is constrained to be  $(1.8_{-0.5}^{+1.0}) \times 10^6 M_\odot$ , and the spin is constrained to be between -0.62 and 0.97; the inclination is constrained to be  $> 78^\circ$ . We conclude that the results from our modelling of the early-time XMM#1, XMM#2, and *NICER* data are consistent with those from the late period, and therefore, that the assumption in the `slimdz` model that the disc lies in the equatorial plane of the BH spin is not the dominant factor in the uncertainty in the parameter estimation.

Furthermore, when using the `slimdz` model to describe the spectrum emitted by a mis-aligned disc during the alignment process, the best-fit spin value derived from modelling could deviate from the true BH spin, and vary between epochs. We test and find that, due to the data quality, it is not possible to constrain the spin value using the `slimdz` for individual epochs when we treat the spin as a free parameter in our fits of the early-time *NICER* data. Together with the above tests, and the consistent mass constraint from the  $M - \sigma_*$  relation, we conclude that the uncertainties in parameter constraints in our study are dominated by the statistical uncertainty of the data instead of our model assumptions on the early-time spectra with `slimdz`.

Moreover, we do not consider the possibility of a warped disc in our study. Such a warp could happen during the disc alignment phase (e.g., [Franchini et al. 2016](#); [White et al. 2019](#)), although it is important to realise that the TDE discs are much smaller than AGN and X-ray binary discs (when expressed in Schwarzschild radii). As suggested by pioneering numerical simulations on accretion discs

**Table 5.** Different fit functions used in this paper to fit the *NICER* data in the early–time period. In total, there are 206 spectra to be fit.  $kT_{\text{zbb}}$  and  $\text{norm}_{\text{zbb}}$  are the temperature and the normalisation of a black body model, respectively. See the text for more details. Histograms of the C-stat/d.o.f. from each test are presented in Fig. A12

| No. | Model                | Free parameter                                      | Fixed parameter  | Number of good–fits (C-stat/d.o.f. < 2) |
|-----|----------------------|---|--|---|
| 1   | TBabs*slimdz         | $\dot{m}, \theta$                                   | $N_{\text{H},G} = 1 \times 10^{20} \text{cm}^{-2}, M_{\bullet} = 7 \times 10^5 M_{\odot}, a_{\bullet} = 0.9$   | 108                                     |
| 2   | TBabs*thcomp*slimdz  | $\dot{m}, kT_e$                                     | $N_{\text{H},G} = 1 \times 10^{20} \text{cm}^{-2}, M_{\bullet} = 7 \times 10^5 M_{\odot}, a_{\bullet} = 0.9, f_c = 1, \tau = 20, \theta = 74^{\circ}$                              | 59                                      |
| 3   |                      | $\theta, kT_e$                                      | $N_{\text{H},G} = 1 \times 10^{20} \text{cm}^{-2}, M_{\bullet} = 7 \times 10^5 M_{\odot}, a_{\bullet} = 0.9, f_c = 1, \tau = 20, \dot{m} = 30 \dot{m}_{\text{Edd}}$                | 165                                     |
| 4   |                      | $\theta, \tau$                                      | $N_{\text{H},G} = 1 \times 10^{20} \text{cm}^{-2}, M_{\bullet} = 7 \times 10^5 M_{\odot}, a_{\bullet} = 0.9, f_c = 1, kT_e = 0.3 \text{ keV}, \dot{m} = 30 \dot{m}_{\text{Edd}}$   | 153                                     |
| 5   |                      | $\theta, kT_e$                                      | $N_{\text{H},G} = 1 \times 10^{20} \text{cm}^{-2}, M_{\bullet} = 7 \times 10^5 M_{\odot}, a_{\bullet} = 0.9, f_c = 0.5, \tau = 20, \dot{m} = 30 \dot{m}_{\text{Edd}}$              | 152                                     |
| 6   |                      | $\theta, f_c$                                       | $N_{\text{H},G} = 1 \times 10^{20} \text{cm}^{-2}, M_{\bullet} = 7 \times 10^5 M_{\odot}, a_{\bullet} = 0.9, \tau = 20, kT_e = 0.3 \text{ keV}, \dot{m} = 30 \dot{m}_{\text{Edd}}$ | 140                                     |
| 7   |                      | $\theta, kT_e$                                      | $N_{\text{H},G} = 1 \times 10^{20} \text{cm}^{-2}, M_{\bullet} = 5 \times 10^5 M_{\odot}, a_{\bullet} = 0.2, f_c = 1, \tau = 20, \dot{m} = 30 \dot{m}_{\text{Edd}}$                | 160                                     |
| 8   | TBabs*(slimdz+zbody) | $\theta, kT_{\text{zbb}}, \text{norm}_{\text{zbb}}$ | $M_{\bullet} = 7 \times 10^5 M_{\odot}, a_{\bullet} = 0.9, \dot{m} = 30 \dot{m}_{\text{Edd}}$  | 115                                     |

(e.g., White et al. 2019; Liska et al. 2023), the disc warp and the disc twist make it possible that, when the inner part of the disc precesses to the phase of minimum inclination (i.e., the inner disc region is face–on), the outer part of the disc is at a different phase so that it intersects our line of sight to the inner disc region and obscures radiations coming from that region. In this sense, the non–planarity of the disc introduces a temporary disc self–obscuration of the inner disc region that will reduce the peak X-ray flux. In such a case, using a planar disc model to fit a warp disc will result in an under–estimation of the amplitude of the inclination variation. However, quantifying the impact of warp on the disc spectrum and the black hole measurements require further studies that incorporate the slim disc and the ray–tracing effects, which we defer to future studies.

From our spectral fits to the X-ray data obtained in the “late period,” we find an accretion rate  $\dot{m} > 3.3 \dot{m}_{\text{Edd}}$  (Table 3), indicating that the source remains at super–Eddington levels throughout the first several hundred days after its detection. This behaviour is consistent with our BH mass constraint of  $M_{\bullet} \sim 10^6 M_{\odot}$ . Theory predicts that TDEs arising from such a BH tend to stay at super–Eddington levels for more than hundreds of days (Stone & Metzger 2016; Wen et al. 2020).

An IC component from a corona describes the spectrum well during the late period (Table 3). This corona is not necessarily the same as the Comptonising medium detected in the early period. We do not refer to the one detected in the early period as a “corona” to mark the potential difference. In the late period, the source develops a corona characterised by an optical depth  $\tau = 8 \pm 3$  and a  $kT_e = 2.4^{+1.4}_{-0.7}$  keV. The appearance of a coronal component when the disc accretion rate remains above the Eddington mass accretion rate has also been found in the TDE 3XMM J150052.0+015452 (J150052; Cao et al. 2023). The coronal temperature in AT2020ocn ( $2.4^{+1.4}_{-0.7}$  keV) is consistent with that in J150052 ( $2.3^{+2.7}_{-0.8}$  keV). The magnetic field in the disc might be critical to power such a corona (e.g., Ghisellini et al. 1988; Merloni & Fabian 2001; Veledina et al. 2011; Beloborodov 2017). It is possible that the electron temperature of the Comptonising medium in the late period is order–of–magnitude larger than that in the early period. As mentioned earlier, the dominant mechanism powering the Comptonising medium might be different between the

early and the late period, since the physical properties of the accretion system (e.g., magnetic field) can be much changed as the disc stops precessing and the accretion rate decreases. In the late period, the disc luminosity decreases as the accretion rate decreases, leading to less cooling of the corona through inverse–Comptonisation, that might also contribute to a hotter corona.

The development of a corona also leads to its emission being reflected from the disc, which is taken into account in our fit in an approximate way by using the `relxillCp` model. The emissivity index  $q$  is constrained to be shallow ( $< 3$ ), which might indicate an extended geometry of the corona or a thick disc (e.g., Mundo et al. 2020). Ezhikode et al. (2020) have found that many AGN in Seyfert I galaxies also have a shallow emissivity (fig. 5 in their paper). Therefore, a shallow emissivity index in AT2020ocn in the late period is not without precedent. The fit also suggest a high inclination of the system ( $81^{+4}_{-7}$  degree) during the XMM#3 epoch. This inclination value is consistent with the highest value ( $\sim 74^{\circ}$ ) found during the disc alignment phase, within  $2\sigma$  error range (and marginally at  $1\sigma$  error range). After the disc alignment is completed, the disc rests at the high inclination.

As a comparison, the IC process contributes  $< 34\%$  of the source flux in the 0.3–1.1 keV band at early epochs, while, at XMM#3, the photons directly from the corona and from the reflection component contribute 64% of the flux in the 0.3–1.1 keV band. Together with the evidence of the hardness ratio (Fig. 2), we conclude that during the first 500 days after its detection, AT2020ocn transits from a soft, disc–dominated spectral state to a hard, corona–dominated spectral state. Spectral state transitions involving a varying coronal component are also observed in other TDEs (e.g., Bade et al. 1996; Komossa et al. 2004; Wevers et al. 2019a; Jonker et al. 2020; Wevers et al. 2021; Cao et al. 2023). Similarly, many ULXs are believed to be powered by high/super–Eddington accretion onto stellar–mass BHs in X–ray binaries (e.g., Gladstone et al. 2009; Motta et al. 2012; Sutton et al. 2013). The strengthening/weakening of a coronal component, when the source accretes at about or at super–Eddington rates, is critical to explain spectral state transitions in ULXs (e.g., Sutton et al. 2013; Feng et al. 2016; Kaaret et al. 2017; Barra et al. 2022). Our findings in AT2020ocn provide further evidence that a

varying coronal component might be common in systems accreting at about or at super–Eddington rates.

The UV light curves of AT2020ocn show no flares but instead only a gradual decay (Fig. 1). This is similar to the UV light curve behaviour observed in other TDEs (e.g., van Velzen et al. 2020). Assuming a slim disc as observed by XMM-Newton (Table 2), we estimate the UV flux of the disc to be an order-of-magnitude lower ( $\lesssim 10^{-29}$  erg/s/cm<sup>2</sup>/Hz with a disc outer radius of  $2R_t \approx 117R_g$ ) than what is observed by Swift/UVOT during the X-ray early period (Fig. 1). Similarly, the observed early-time (within several hundred of days after the initial disruption) UV flux in several other TDEs is higher than the expected disc UV flux (e.g., Mummery & Balbus 2020; Mummery et al. 2023; Wen et al. 2023). The decoupling of X-rays and UV (flaring and non-flaring) is also seen in other TDEs (e.g., Pasham et al. 2021; Evans et al. 2023; Guolo et al. 2023). It is not possible to distinguish different UV emission mechanisms (e.g., self-intersection shocks in debris streams or a layer reprocessing the X-rays from the inner accretion region) in MOSFIT, which is agnostic about the emission mechanism and only assumes an efficiency  $\epsilon$  for the fraction of accretion energy converted to the bolometric luminosity  $L = \epsilon \dot{M}_{\text{acc}} c^2$  ( $\dot{M}_{\text{acc}}(t)$  is the accretion rate from viscously delayed fall-back mass accretion  $\dot{M}_{\text{fb}}(t)$ , see also Section 3.4). The  $\epsilon$  is treated as a time-independent, free parameter in our UV modelling and is found to be  $\sim 10^{-3}$  (Table 4). The energy emitted by the UV photons is similar to our estimate of the energy dissipated in the circularisation process<sup>8</sup> ( $\gtrsim 0.007 \dot{M}_{\text{fb}} c^2$ ). It is possible that the circularisation process plays an important role in powering the early-time UV emission.

Overall, our analysis combining the UV and X-ray data is consistent with the picture where the X-ray flares arise from the inner accretion disc, whose inclination varies during the disc alignment process, while the UV emission comes from another mechanism. Recently, Mummery et al. (2024) developed a method using the late-time UV data to constrain the BH mass in a TDE. For this method to be applicable, it is important that the source has reached a “plateau phase” in UV in the late time of the TDE (e.g., Inkenhaag et al. 2023; Mummery et al. 2024), and that the disc emission dominates the detected UV emission. Even though the current UV data is not sufficient to tell if this state is achieved before the end of the observed period, it would be interesting to see if the UV scaling method can provide a mass estimation for the AT2020ocn similar to our result or the  $M - \sigma_*$  result using future deep UV observations.

## 5 CONCLUSIONS

In this paper, we present our analysis of the X-ray and UV data of TDE AT2020ocn observed by NICER, XMM-Newton, and Swift. The X-ray lightcurve shows strong flares in the first  $\approx 100$  days, while, over the same period, the UV emission decays gradually. From our X-ray spectral fits using a slim disc model, we constrain the BH mass to be  $(7^{+13}_{-3}) \times 10^5 M_\odot$  at the  $1\sigma$  (68%) confidence level. This mass is consistent with that derived from the analysis of the UV light curve,  $\log(M_\bullet/M_\odot) \sim 6.2 \pm 0.3$ , and with that derived from the  $M - \sigma_*$  relation,  $\log(M_\bullet/M_\odot) \sim 6.4 \pm 0.6$ .

We find that the disc alignment process might well be responsible

<sup>8</sup> A lower limit on the dissipated energy in the circularisation process is estimated, in an order-of-magnitude way, by comparing the orbital energy of the fallback orbit of the most tightly bound debris (major axis  $\sim 10^3 R_g$ ; Rees 1988) to the orbital energy of a circularised orbit of radius  $2R_t \approx 117R_g$  at the disc outer edge (Franchini et al. 2016).

for the qualitatively different behaviour of the X-ray and UV light curves with X-ray flares while the UV emission decays gradually. In particular:

- The early XMM-Newton/EPIC-pn spectra can be well-fit by the slim disc emission. The X-ray flares observed by NICER can arise from a combination of a varying disc inclination and a varying inverse-Comptonisation component.
- We explain the inclination variation in this TDE by proposing that the disc alignment is ongoing, which requires that the orbital angular momentum vector of the star prior to disruption is misaligned from the BH spin angular momentum vector. The inner part of the tilted disc is drawn into the BH equatorial plane due to a combination of the Bardeen–Petterson effect and internal torques. This alignment process causes the inner disc to temporarily precess, explaining the observed inclination variations.
- The observed spectral variations during the X-ray flares can be explained by the slim disk model convolved with the effect of inverse-Comptonisation. The contribution of the inverse-Comptonisation process to the observed spectrum increases with increasing X-ray photon count rate, consistent with observing more up-scattered photons from the inner accretion region as the inclination decreases.
- The UV light curves for AT2020ocn show no evidence for flares but instead only a gradual decay similar to the UV light curves of other TDEs. Most of the UV light likely originates from somewhere other than the accretion disk. The amount of energy emitted in the UV bands is similar to the estimate of that dissipated in the circularisation process.
- After the period of X-ray flares, the source spectrum becomes much harder. While the mass accretion rate remains at super-Eddington levels, a corona with an optical depth  $\tau = 8 \pm 3$  and an electron temperature  $2.4^{+1.4}_{-0.7}$  keV forms after  $\sim 300$  days. We interpret the late-time XMM-Newton/EPIC-pn spectrum as a combination of disc emission, coronal emission, and emission reflected off the disc. Our findings in AT2020ocn provide further evidence that a varying coronal component might be common in systems accreting at about or at super-Eddington rates.

## ACKNOWLEDGEMENTS

We thank the anonymous referee for insightful comments. This work used the Dutch national e-infrastructure with the support of the SURF Cooperative using grant no. EINF-3954. This work made use of data supplied by the UK Swift Science Data Centre at the University of Leicester. AIZ acknowledges support from NASA ADAP grant #80NSSC21K0988.

## DATA AVAILABILITY

All the X-ray data in this paper are publicly available from the HEASARC data archive (<https://heasarc.gsfc.nasa.gov/>). A reproduction package is available at DOI: 10.5281/zenodo.11162299.

## REFERENCES

- Abramowicz M., Czerny B., Lasota J., Szuszkiewicz E., 1988, The Astrophysical Journal, 332, 646
- Aghanim N., et al., 2020, Astronomy & Astrophysics, 641, A6
- Akaïke H., 1974, IEEE transactions on automatic control, 19, 716
- Andalman Z. L., Liska M. T., Tchekhovskoy A., Coughlin E. R., Stone N., 2022, Monthly Notices of the Royal Astronomical Society, 510, 1627

- Arnaud K., 1996, in *Astronomical Data Analysis Software and Systems V*, p. 17
- Auchettl K., Guillochon J., Ramirez-Ruiz E., 2017, *The Astrophysical Journal*, 838, 149
- Bade N., Komossa S., Dahlem M., 1996, *Astronomy and Astrophysics*, 309, L35
- Barra F., et al., 2022, *Monthly Notices of the Royal Astronomical Society*, 516, 3972
- Belloni T. M., 2010, in , *The Jet Paradigm*. Springer, pp 53–84
- Beloborodov A. M., 2017, *The Astrophysical Journal*, 850, 141
- Bonnerot C., Lu W., 2020, *Monthly Notices of the Royal Astronomical Society*, 495, 1374
- Cao Z., Jonker P., Wen S., Stone N., Zabludoff A., 2023, *Monthly Notices of the Royal Astronomical Society*, 519, 2375
- Cash W., 1979, *The Astrophysical Journal*, 228, 939
- Chen Y.-P., et al., 2022, *The Astrophysical Journal*, 936, 46
- Dai L., McKinney J. C., Roth N., Ramirez-Ruiz E., Miller M. C., 2018, *The Astrophysical Journal Letters*, 859, L20
- Dai X., Kong L., Bu Q., Santangelo A., Zhang S., Ji L., Zhang S., Yorgancioglu E. S., 2023, *Monthly Notices of the Royal Astronomical Society*, 521, 2692
- Dauser T., García J., Parker M., Fabian A., Wilms J., 2014, *Monthly Notices of the Royal Astronomical Society: Letters*, 444, L100
- Done C., Kubota A., 2006, *Monthly Notices of the Royal Astronomical Society*, 371, 1216
- Evans C. R., Kochanek C. S., 1989, *The Astrophysical Journal*, 346, L13
- Evans P., et al., 2009, *Monthly Notices of the Royal Astronomical Society*, 397, 1177
- Evans P., et al., 2023, *Nature Astronomy*, 7, 1368
- Ezhikode S. H., Dewangan G. C., Misra R., Philip N. S., 2020, *Monthly Notices of the Royal Astronomical Society*, 495, 3373
- Feng H., Tao L., Kaaret P., Grisé F., 2016, *The Astrophysical Journal*, 831, 117
- Fragile P. C., Anninos P., 2005, *The Astrophysical Journal*, 623, 347
- Fragile P. C., Blaes O. M., Anninos P., Salmonson J. D., 2007, *The Astrophysical Journal*, 668, 417
- Franchini A., Lodato G., Facchini S., 2016, *Monthly Notices of the Royal Astronomical Society*, 455, 1946
- García J., et al., 2014, *The Astrophysical Journal*, 782, 76
- Gelman A., Rubin D. B., 1992, *Statistical science*, pp 457–472
- Gezari S., 2021, *Annual Review of Astronomy and Astrophysics*, 59, 21
- Gezari S., et al., 2006, *The Astrophysical Journal*, 653, L25
- Gezari S., Velzen S. v., Stern D., Frederick S., Hammerstein E., Ward C., Cenko S., Graham M., 2020, *The Astronomer's Telegram*, 13859, 1
- Ghisellini G., Guilbert P. W., Svensson R., 1988, *The Astrophysical Journal*, 334, L5
- Gladstone J. C., Roberts T. P., Done C., 2009, *Monthly Notices of the Royal Astronomical Society*, 397, 1836
- Graham M. J., et al., 2019, *Publications of the Astronomical Society of the Pacific*, 131, 078001
- Guillochon J., Ramirez-Ruiz E., 2013, *The Astrophysical Journal*, 767, 25
- Guillochon J., Nicholl M., Villar V. A., Mockler B., Narayan G., Mandel K. S., Berger E., Williams P. K., 2018, *The Astrophysical Journal Supplement Series*, 236, 6
- Guolo M., et al., 2023, *arXiv preprint arXiv:2309.03011*
- Hills J. G., 1975, *Nature*, 254, 295
- Inkenhaag A., Jonker P. G., Levan A. J., Chrimes A. A., Mummery A., Perley D. A., Tanvir N. R., 2023, *Monthly Notices of the Royal Astronomical Society*, 525, 4042
- Jiang Y.-F., Stone J. M., Davis S. W., 2019, *The Astrophysical Journal*, 880, 67
- Jonker P., Stone N., Generozov A., van Velzen S., Metzger B., 2020, *The Astrophysical Journal*, 889, 166
- Kaaret P., Feng H., Roberts T. P., 2017, *Annu. Rev. Astron. Astrophys.*, 55, 303
- Kaastra J., Bleeker J., 2016, *Astronomy & Astrophysics*, 587, A151
- Kara E., Dai L., Reynolds C., Kallman T., 2018, *Monthly Notices of the Royal Astronomical Society*, 474, 3593
- Katayama H., Takahashi I., Ikebe Y., Matsushita K., Freyberg M., 2004, *Astronomy & Astrophysics*, 414, 767
- Kitaki T., Mineshige S., Ohsuga K., Kawashima T., 2021, *Publications of the Astronomical Society of Japan*, 73, 450
- Komossa S., Halpern J., Schartel N., Hasinger G., Santos-Lleo M., Predehl P., 2004, *The Astrophysical Journal Letters*, 603, L17
- Kubota A., Done C., 2019, *Monthly Notices of the Royal Astronomical Society*, 489, 524
- Lin D., et al., 2017, *Nature Astronomy*, 1, 1
- Lin D., et al., 2020, *The Astrophysical Journal Letters*, 892, L25
- Liska M., Hesp C., Tchekhovskoy A., Ingram A., van der Klis M., Markoff S., 2018, *Monthly Notices of the Royal Astronomical Society: Letters*, 474, L81
- Liska M., Kaaz N., Musoke G., Tchekhovskoy A., Porth O., 2023, *The Astrophysical Journal Letters*, 944, L48
- Liu Z., et al., 2023, *Astronomy & Astrophysics*, 669, A75
- Lodato G., Rossi E. M., 2011, *Monthly Notices of the Royal Astronomical Society*, 410, 359
- Loeb A., Ulmer A., 1997, *The Astrophysical Journal*, 489, 573
- Lomb N. R., 1976, *Astrophysics and space science*, 39, 447
- Magdziarz P., Blaes O. M., Zdziarski A. A., Johnson W. N., Smith D. A., 1998, *Monthly Notices of the Royal Astronomical Society*, 301, 179
- Masterson M., et al., 2022, *The Astrophysical Journal*, 934, 35
- Merloni A., Fabian A., 2001, *Monthly Notices of the Royal Astronomical Society*, 321, 549
- Metzger B. D., Stone N. C., 2016a, *MNRAS*, 461, 948
- Metzger B. D., Stone N. C., 2016b, *Monthly Notices of the Royal Astronomical Society*, 461, 948
- Middleton M. J., Walton D. J., Roberts T. P., Heil L., 2013, *Monthly Notices of the Royal Astronomical Society: Letters*, 438, L51
- Miller J., Reynolds M., 2020, *The Astronomer's Telegram*, 13863, 1
- Mockler B., Guillochon J., Ramirez-Ruiz E., 2019, *The Astrophysical Journal*, 872, 151
- Motta S., Homan J., Munoz-Darias T., Casella P., Belloni T., Hiemstra B., Méndez M., 2012, *Monthly Notices of the Royal Astronomical Society*, 427, 595
- Mummery A., Balbus S. A., 2020, *Monthly Notices of the Royal Astronomical Society*, 492, 5655
- Mummery A., Balbus S. A., 2021, *Monthly Notices of the Royal Astronomical Society*, 504, 4730
- Mummery A., Wevers T., Saxton R., Pasham D., 2023, *Monthly Notices of the Royal Astronomical Society*, 519, 5828
- Mummery A., van Velzen S., Nathan E., Ingram A., Hammerstein E., Fraser-Talente L., Balbus S., 2024, *Monthly Notices of the Royal Astronomical Society*, 527, 2452
- Mundo S. A., et al., 2020, *Monthly Notices of the Royal Astronomical Society*, 496, 2922
- Ohsuga K., Mineshige S., 2011, *The Astrophysical Journal*, 736, 2
- Page D. N., Thorne K. S., 1974, *The Astrophysical Journal*, 191, 499
- Pasham D. R., et al., 2021, *Nature Astronomy*, 6, 249
- Pasham D. R., et al., 2023, *Nature Astronomy*, 7, 88
- Pasham D. R., et al., 2024, *arXiv preprint arXiv:2402.09689*
- Pinto C., Middleton M. J., Fabian A. C., 2016, *Nature*, 533, 64
- Pinto C., et al., 2021, *Monthly Notices of the Royal Astronomical Society*, 505, 5058
- Piran T., Svirski G., Krolik J., Cheng R. M., Shiokawa H., 2015, *The Astrophysical Journal*, 806, 164
- Rees M. J., 1988, *Nature*, 333, 523
- Remillard R. A., et al., 2022, *AJ*, 163, 130
- Roming P. W., et al., 2005, *Space Science Reviews*, 120, 95
- Roth N., Kasen D., 2018, *The Astrophysical Journal*, 855, 54
- Roth N., Rossi E. M., Krolik J., Piran T., Mockler B., Kasen D., 2020, *Space Science Reviews*, 216, 1
- Ryu T., Krolik J., Piran T., 2020, *The Astrophysical Journal*, 904, 73
- Sądowski A., 2009, *The Astrophysical Journal Supplement Series*, 183, 171
- Sądowski A., Abramowicz M., Bursa M., Kluźniak W., Lasota J.-P., Różańska A., 2011, *Astronomy & Astrophysics*, 527, A17
- Saxton R., et al., 2014, *Astronomy & Astrophysics*, 572, A1

- Saxton R., Read A. M., Komossa S., Lira P., Alexander K., Wieringa M., 2017, *Astronomy & Astrophysics*, 598, A29
- Saxton R., et al., 2019, *Astronomy & Astrophysics*, 630, A98
- Saxton R., Komossa S., Auchettl K., Jonker P., 2020, *Space Science Reviews*, 216, 1
- Scargle J. D., 1982, *Astrophysical Journal*, 263, 835
- Schlafly E. F., Finkbeiner D. P., 2011, *The Astrophysical Journal*, 737, 103
- Shakura N. I., Sunyaev R. A., 1973, *Astronomy and Astrophysics*, 24, 337
- Shappee B. J., et al., 2014, *The Astrophysical Journal*, 788, 48
- Shiokawa H., Krolik J. H., Cheng R. M., Piran T., Noble S. C., 2015, *The Astrophysical Journal*, 804, 85
- Steinberg E., Stone N. C., 2022, arXiv preprint arXiv:2206.10641
- Stone N. C., 2015, *The Tidal Disruption of Stars by Supermassive Black Holes: An Analytic Approach*, doi:10.1007/978-3-319-12676-0.
- Stone N., Loeb A., 2012, *Physical Review Letters*, 108, 061302
- Stone N. C., Metzger B. D., 2016, *Monthly Notices of the Royal Astronomical Society*, 455, 859
- Strubbe L. E., Quataert E., 2009, *Monthly Notices of the Royal Astronomical Society*, 400, 2070
- Sutton A. D., Roberts T. P., Middleton M. J., 2013, *Monthly Notices of the Royal Astronomical Society*, 435, 1758
- Takeuchi S., Ohsuga K., Mineshige S., 2013, *Publications of the Astronomical Society of Japan*, 65, 88
- Tchekhovskoy A., Metzger B. D., Giannios D., Kelley L. Z., 2014, *Monthly Notices of the Royal Astronomical Society*, 437, 2744
- Teboul O., Metzger B. D., 2023, arXiv preprint arXiv:2308.05161
- Tony J., et al., 2018, *Publications of the Astronomical Society of the Pacific*, 130, 064505
- Tripathi P., Dewangan G. C., 2022, *The Astrophysical Journal*, 930, 117
- Ulmer A., 1999, *The Astrophysical Journal*, 514, 180
- Van Velzen S., et al., 2019, *The Astrophysical Journal*, 872, 198
- Veledina A., Vurm I., Poutanen J., 2011, *Monthly Notices of the Royal Astronomical Society*, 414, 3330
- Watanabe S., Opper M., 2010, *Journal of machine learning research*, 11
- Wen S., Wang S., Luo X., 2018, *Journal of Cosmology and Astroparticle Physics*, 2018, 011
- Wen S., Jonker P. G., Stone N. C., Zabludoff A. I., Psaltis D., 2020, *The Astrophysical Journal*, 897, 80
- Wen S., Jonker P. G., Stone N. C., Zabludoff A. I., Cao Z., 2022, arXiv preprint arXiv:2204.03922
- Wen S., Jonker P. G., Stone N. C., Van Velzen S., Zabludoff A. I., 2023, *Monthly Notices of the Royal Astronomical Society*, 522, 1155
- Wevers T., et al., 2019a, *Monthly Notices of the Royal Astronomical Society*, 487, 4136
- Wevers T., et al., 2019b, *Monthly Notices of the Royal Astronomical Society*, 488, 4816
- Wevers T., et al., 2021, *The Astrophysical Journal*, 912, 151
- White C. J., Quataert E., Blaes O., 2019, *The Astrophysical Journal*, 878, 51
- Wilkins D., Gallo L. C., 2015, *Monthly Notices of the Royal Astronomical Society*, 448, 703
- Wilms J., Allen A., McCray R., 2000, *The Astrophysical Journal*, 542, 914
- Yang H., Yuan F., Kwan T., Dai L., 2023, *Monthly Notices of the Royal Astronomical Society*, 523, 208
- Yao Y., et al., 2022, *The Astrophysical Journal*, 937, 8
- Zanazzi J., Lai D., 2019, *Monthly Notices of the Royal Astronomical Society*, 487, 4965
- Zdziarski A. A., Johnson W. N., Magdziarz P., 1996, *Monthly Notices of the Royal Astronomical Society*, 283, 193
- Zdziarski A. A., Szanecki M., Poutanen J., Gierliński M., Biernacki P., 2020, *Monthly Notices of the Royal Astronomical Society*, 492, 5234
- van Velzen S., et al., 2011, *The Astrophysical Journal*, 741, 73
- van Velzen S., Holoiën T. W.-S., Onori F., Hung T., Arcavi I., 2020, *Space Science Reviews*, 216, 1



**Table A1.** *Swift* observations used for the MOSFiT analysis of the UV data in Section 3.4.

| Observation ID | Date       | XRT exposure (s) | UVOT exposure (s) |
|----------------|------------|------------------|-------------------|
| 00013592001    | 2020-06-25 | 2200             | 2167              |
| 00013592002    | 2020-07-02 | 1612             | 1595              |
| 00013592003    | 2020-07-09 | 1885             | 1824              |
| 00013608001    | 2020-07-11 | 4958             | 4948              |
| 00013608002    | 2020-07-11 | 3977             | 3916              |
| 00013608003    | 2020-07-13 | 4983             | 4920              |
| 00013608005    | 2020-07-15 | 4701             | 4693              |
| 00013592004    | 2020-07-16 | 568              | 567               |
| 00013608006    | 2020-07-16 | 4483             | 4477              |
| 00013608007    | 2020-07-17 | 4603             | 4601              |
| 00013608008    | 2020-07-18 | 995              | 987               |
| 00013608009    | 2020-07-19 | 241              | 240               |
| 00013608010    | 2020-07-20 | 933              | 911               |
| 00013592005    | 2020-07-21 | 1402             | 1383              |
| 00013608011    | 2020-07-22 | 943              | 929               |
| 00013592006    | 2020-07-23 | 2208             | 2175              |
| 00013608012    | 2020-07-23 | 1003             | 990               |
| 00013608013    | 2020-07-24 | 835              | 823               |
| 00013608014    | 2020-07-31 | 963              | 952               |
| 00013608016    | 2020-08-04 | 827              | 816               |
| 00013608017    | 2020-08-06 | 905              | 895               |
| 00013608018    | 2020-08-08 | 938              | 924               |
| 00013608019    | 2020-08-10 | 1058             | 1047              |
| 00013608020    | 2020-08-20 | 1665             | 1640              |
| 00013608021    | 2020-08-22 | 1138             | 1127              |
| 00013608022    | 2020-08-24 | 1803             | 1779              |
| 00013608023    | 2020-08-26 | 1316             | 1304              |
| 00013608024    | 2020-08-28 | 1729             | 1706              |
| 00013608025    | 2020-08-30 | 1637             | 1624              |
| 00013608026    | 2020-09-01 | 1597             | 0                 |
| 00013608027    | 2020-09-03 | 2088             | 2054              |
| 00013608028    | 2020-09-05 | 2055             | 2003              |
| 00013608029    | 2020-09-12 | 1443             | 1432              |
| 00013608030    | 2020-09-15 | 915              | 910               |
| 00013608031    | 2020-09-18 | 1672             | 1649              |
| 00013608032    | 2020-09-21 | 998              | 986               |
| 00013608033    | 2020-09-24 | 1382             | 1370              |
| 00013608034    | 2020-09-27 | 1363             | 1351              |
| 00013608035    | 2020-09-30 | 1413             | 1400              |
| 00013608036    | 2020-10-03 | 1387             | 1375              |
| 00013608037    | 2020-10-06 | 1038             | 1025              |
| 00013608038    | 2020-10-09 | 313              | 303               |
| 00013608039    | 2020-10-11 | 1401             | 1368              |
| 00013608040    | 2020-10-15 | 1850             | 1827              |
| 00013608041    | 2020-10-18 | 1680             | 1668              |
| 00013608042    | 2020-10-21 | 268              | 267               |
| 00013608043    | 2020-10-23 | 346              | 482               |
| 00013608044    | 2020-10-27 | 1256             | 1243              |
| 00013608046    | 2020-11-02 | 2174             | 2152              |
| 00013608047    | 2020-11-05 | 1951             | 1885              |
| 00013608048    | 2020-11-08 | 2136             | 2102              |
| 00013608049    | 2020-11-08 | 1988             | 1967              |
| 00013608050    | 2020-11-11 | 1842             | 1807              |
| 00013608051    | 2020-11-14 | 1434             | 1423              |
| 00013608052    | 2020-11-17 | 2023             | 2002              |
| 00013608053    | 2020-11-20 | 1908             | 1886              |
| 00013608054    | 2020-11-27 | 868              | 856               |
| 00013608055    | 2020-11-30 | 835              | 823               |

Continuation of Table A1

|             |            |      |      |
|-------------|------------|------|------|
| 00013608056 | 2020-12-03 | 955  | 943  |
| 00013608057 | 2020-12-10 | 873  | 860  |
| 00013608059 | 2020-12-18 | 880  | 868  |
| 00013608060 | 2020-12-21 | 653  | 643  |
| 00013608061 | 2020-12-24 | 980  | 969  |
| 00013608062 | 2021-02-24 | 707  | 696  |
| 00013608063 | 2021-02-27 | 940  | 930  |
| 00013608064 | 2021-03-02 | 537  | 531  |
| 00013608065 | 2021-03-05 | 955  | 933  |
| 00013608066 | 2021-03-11 | 903  | 880  |
| 00013608067 | 2021-03-14 | 1063 | 1040 |
| 00013608068 | 2021-03-20 | 855  | 843  |
| 00013608069 | 2021-03-23 | 1068 | 1056 |
| 00013608070 | 2021-05-28 | 68   | 67   |
| 00013608071 | 2021-05-31 | 1738 | 1715 |
| 00013608072 | 2021-06-06 | 1695 | 1683 |
| 00013608073 | 2021-06-18 | 1259 | 1225 |
| 00013608074 | 2021-06-21 | 1786 | 1744 |

End of Table

**Table A2.** List of per-GTI-based *NICER* spectra used for the spectral analysis in Section 3.3.2.

| Observation ID | Date                | GTI duration (s) | Estimated Source Count Rate (count /s) |
|----------------|---------------------|------------------|--|
| 3201670101     | 2020-07-11 01:44:46 | 483.0            | 0.97 ± 0.05                            |
| 3201670101     | 2020-07-11 03:17:28 | 373.0            | 1.22 ± 0.06                            |
| 3201670102     | 2020-07-12 04:03:47 | 1717.0           | 1.95 ± 0.04                            |
| 3201670102     | 2020-07-12 21:11:06 | 332.0            | 1.98 ± 0.08                            |
| 3201670103     | 2020-07-13 12:34:07 | 1216.0           | 1.23 ± 0.03                            |
| 3201670108     | 2020-07-18 11:46:49 | 342.0            | 0.45 ± 0.05                            |
| 3201670114     | 2020-07-24 11:47:06 | 1665.0           | 1.18 ± 0.03                            |
| 3201670114     | 2020-07-24 21:04:25 | 1196.0           | 1.43 ± 0.04                            |
| 3201670115     | 2020-07-25 00:10:25 | 1276.0           | 1.46 ± 0.04                            |
| 3201670115     | 2020-07-25 06:22:05 | 1857.0           | 1.04 ± 0.03                            |
| 3201670115     | 2020-07-25 11:00:50 | 1089.0           | 1.56 ± 0.04                            |
| 3201670115     | 2020-07-25 14:06:29 | 1524.0           | 1.69 ± 0.04                            |
| 3201670116     | 2020-07-26 02:29:45 | 1064.0           | 1.50 ± 0.04                            |
| 3201670118     | 2020-07-28 11:47:45 | 1075.0           | 1.64 ± 0.04                            |
| 3201670118     | 2020-07-28 17:59:20 | 1080.0           | 1.59 ± 0.04                            |
| 3201670118     | 2020-07-28 21:04:55 | 526.0            | 1.45 ± 0.06                            |
| 3201670119     | 2020-07-29 09:28:03 | 1097.0           | 1.90 ± 0.05                            |
| 3201670119     | 2020-07-29 12:34:37 | 507.0            | 1.20 ± 0.06                            |
| 3201670119     | 2020-07-29 18:45:43 | 1077.0           | 1.59 ± 0.04                            |
| 3201670119     | 2020-07-29 21:51:45 | 1075.0           | 1.60 ± 0.04                            |
| 3201670120     | 2020-07-30 00:57:23 | 1077.0           | 1.65 ± 0.04                            |
| 3201670120     | 2020-07-30 04:03:28 | 1072.0           | 1.63 ± 0.04                            |
| 3201670120     | 2020-07-30 13:21:03 | 1077.0           | 1.67 ± 0.04                            |
| 3201670120     | 2020-07-30 16:27:03 | 1057.0           | 1.84 ± 0.05                            |
| 3201670120     | 2020-07-30 19:32:43 | 1077.0           | 1.81 ± 0.05                            |
| 3201670121     | 2020-07-31 07:56:45 | 1035.0           | 1.85 ± 0.05                            |
| 3201670121     | 2020-07-31 17:14:26 | 1034.0           | 1.57 ± 0.04                            |
| 3201670121     | 2020-07-31 20:20:26 | 1033.0           | 1.75 ± 0.05                            |
| 3201670121     | 2020-07-31 23:26:07 | 1045.0           | 2.04 ± 0.05                            |
| 3201670122     | 2020-08-01 02:32:07 | 1033.0           | 1.79 ± 0.05                            |
| 3201670122     | 2020-08-01 05:38:07 | 1029.0           | 2.71 ± 0.06                            |
| 3201670122     | 2020-08-01 11:49:49 | 1031.0           | 2.23 ± 0.05                            |
| 3201670122     | 2020-08-01 14:55:43 | 1031.0           | 2.12 ± 0.05                            |
| 3201670122     | 2020-08-01 21:18:12 | 387.4            | 1.84 ± 0.08                            |
| 3201670123     | 2020-08-02 04:52:09 | 1025.0           | 2.02 ± 0.05                            |
| 3201670123     | 2020-08-02 11:03:48 | 1030.0           | 1.54 ± 0.04                            |
| 3201670123     | 2020-08-02 14:09:47 | 1024.0           | 2.02 ± 0.05                            |
| 3201670123     | 2020-08-02 18:48:03 | 1040.0           | 1.97 ± 0.05                            |
| 3201670123     | 2020-08-02 20:21:27 | 1030.0           | 2.29 ± 0.05                            |
| 3201670123     | 2020-08-02 23:27:27 | 1016.0           | 1.88 ± 0.05                            |
| 3201670124     | 2020-08-03 01:00:26 | 397.0            | 1.45 ± 0.07                            |
| 3201670124     | 2020-08-03 05:39:10 | 1027.0           | 2.08 ± 0.05                            |
| 3201670124     | 2020-08-03 08:45:05 | 1024.0           | 2.29 ± 0.05                            |
| 3201670124     | 2020-08-03 14:56:48 | 1029.0           | 2.16 ± 0.05                            |
| 3201670124     | 2020-08-03 18:02:46 | 1017.0           | 2.22 ± 0.05                            |
| 3201670124     | 2020-08-03 22:41:27 | 1033.0           | 2.36 ± 0.05                            |
| 3201670125     | 2020-08-04 04:53:28 | 1012.0           | 2.10 ± 0.05                            |
| 3201670125     | 2020-08-04 07:59:08 | 1032.0           | 1.82 ± 0.05                            |
| 3201670125     | 2020-08-04 11:05:06 | 1006.0           | 1.67 ± 0.05                            |
| 3201670125     | 2020-08-04 14:11:04 | 1023.0           | 2.54 ± 0.05                            |
| 3201670125     | 2020-08-04 17:16:47 | 988.0            | 2.05 ± 0.05                            |
| 3201670125     | 2020-08-04 20:22:47 | 1028.0           | 2.14 ± 0.05                            |
| 3201670125     | 2020-08-04 23:28:26 | 1043.0           | 2.03 ± 0.05                            |
| 3201670126     | 2020-08-05 04:07:26 | 1033.0           | 2.78 ± 0.06                            |
| 3201670126     | 2020-08-05 07:13:26 | 1027.0           | 2.66 ± 0.06                            |
| 3201670126     | 2020-08-05 10:19:06 | 1034.0           | 2.07 ± 0.05                            |
| 3201670126     | 2020-08-05 13:25:07 | 1033.0           | 2.35 ± 0.05                            |
| 3201670126     | 2020-08-05 16:31:06 | 1030.0           | 2.36 ± 0.05                            |

Continuation of Table A2

|            |                     |        |             |
|------------|---------------------|--------|-------------|
| 3201670126 | 2020-08-05 19:36:47 | 1042.0 | 2.02 ± 0.05 |
| 3201670126 | 2020-08-05 22:42:46 | 1034.0 | 2.50 ± 0.06 |
| 3201670127 | 2020-08-06 01:48:47 | 1030.0 | 2.27 ± 0.05 |
| 3201670127 | 2020-08-06 04:54:27 | 1045.0 | 1.93 ± 0.05 |
| 3201670127 | 2020-08-06 08:00:26 | 1034.0 | 2.29 ± 0.05 |
| 3201670127 | 2020-08-06 11:06:20 | 1040.0 | 2.24 ± 0.05 |
| 3201670127 | 2020-08-06 14:12:06 | 1048.0 | 2.53 ± 0.05 |
| 3201670127 | 2020-08-06 17:18:08 | 1041.0 | 2.23 ± 0.05 |
| 3201670127 | 2020-08-06 20:24:01 | 1038.0 | 2.38 ± 0.05 |
| 3201670127 | 2020-08-06 23:29:47 | 1051.0 | 2.03 ± 0.05 |
| 3201670128 | 2020-08-07 02:35:51 | 1042.0 | 2.54 ± 0.05 |
| 3201670128 | 2020-08-07 05:41:27 | 1036.0 | 1.78 ± 0.05 |
| 3201670128 | 2020-08-07 08:49:41 | 919.0  | 2.64 ± 0.06 |
| 3201670128 | 2020-08-07 11:53:28 | 1048.0 | 1.76 ± 0.05 |
| 3201670128 | 2020-08-07 14:59:05 | 1068.0 | 2.39 ± 0.05 |
| 3201670128 | 2020-08-07 18:05:07 | 1053.0 | 2.77 ± 0.06 |
| 3201670128 | 2020-08-07 21:10:45 | 1075.0 | 2.13 ± 0.05 |
| 3201670129 | 2020-08-08 00:16:45 | 1073.0 | 2.48 ± 0.05 |
| 3201670129 | 2020-08-08 06:28:28 | 1072.0 | 2.50 ± 0.05 |
| 3201670129 | 2020-08-08 12:40:24 | 1076.0 | 2.63 ± 0.05 |
| 3201670129 | 2020-08-08 18:52:08 | 1086.0 | 3.10 ± 0.06 |
| 3201670129 | 2020-08-08 21:57:49 | 1091.0 | 2.93 ± 0.06 |
| 3201670130 | 2020-08-09 01:03:45 | 1095.0 | 3.08 ± 0.06 |
| 3201670130 | 2020-08-09 04:09:46 | 1094.0 | 2.94 ± 0.06 |
| 3201670130 | 2020-08-09 07:16:44 | 1036.0 | 2.90 ± 0.06 |
| 3201670130 | 2020-08-09 11:54:24 | 1116.0 | 3.37 ± 0.06 |
| 3201670130 | 2020-08-09 16:33:08 | 1132.0 | 3.27 ± 0.06 |
| 3201670131 | 2020-08-10 00:17:47 | 1136.0 | 3.17 ± 0.06 |
| 3201670131 | 2020-08-10 04:56:45 | 1155.0 | 3.39 ± 0.06 |
| 3201670131 | 2020-08-10 11:08:27 | 1123.0 | 3.94 ± 0.06 |
| 3201670131 | 2020-08-10 17:20:06 | 1189.0 | 3.73 ± 0.06 |
| 3201670131 | 2020-08-10 20:26:06 | 1198.0 | 2.66 ± 0.05 |
| 3201670132 | 2020-08-11 02:53:42 | 328.0  | 2.99 ± 0.10 |
| 3201670132 | 2020-08-11 05:59:23 | 320.0  | 4.11 ± 0.12 |
| 3201670132 | 2020-08-11 08:49:27 | 1234.0 | 4.05 ± 0.06 |
| 3201670132 | 2020-08-11 16:34:06 | 1294.0 | 3.81 ± 0.06 |
| 3201670133 | 2020-08-12 01:51:47 | 1286.0 | 3.51 ± 0.06 |
| 3201670133 | 2020-08-12 06:30:28 | 1124.0 | 3.91 ± 0.06 |
| 3201670133 | 2020-08-12 12:56:02 | 365.0  | 3.39 ± 0.10 |
| 3201670133 | 2020-08-12 13:02:30 | 363.0  | 3.35 ± 0.10 |
| 3201670133 | 2020-08-12 16:02:01 | 1317.0 | 3.29 ± 0.05 |
| 3201670133 | 2020-08-12 18:54:07 | 773.0  | 3.56 ± 0.08 |
| 3201670133 | 2020-08-12 21:59:48 | 1585.0 | 3.34 ± 0.05 |
| 3201670133 | 2020-08-12 23:32:45 | 1308.0 | 2.85 ± 0.05 |
| 3201670134 | 2020-08-13 02:38:45 | 1359.0 | 3.28 ± 0.05 |
| 3201670134 | 2020-08-13 04:11:45 | 918.0  | 3.32 ± 0.07 |
| 3201670134 | 2020-08-13 07:17:27 | 1203.0 | 2.97 ± 0.05 |
| 3201670134 | 2020-08-13 10:23:26 | 1257.0 | 2.64 ± 0.05 |
| 3201670134 | 2020-08-13 16:35:05 | 1277.0 | 2.39 ± 0.05 |
| 3201670134 | 2020-08-13 22:46:47 | 1170.0 | 1.62 ± 0.04 |
| 3201670134 | 2020-08-13 23:06:44 | 496.0  | 1.61 ± 0.07 |
| 3201670135 | 2020-08-14 18:54:44 | 1436.0 | 0.85 ± 0.03 |
| 3201670137 | 2020-08-16 09:38:08 | 1375.0 | 0.76 ± 0.03 |
| 3201670140 | 2020-08-19 05:46:48 | 2083.0 | 0.65 ± 0.02 |
| 3201670140 | 2020-08-19 10:49:10 | 682.0  | 0.61 ± 0.04 |
| 3201670141 | 2020-08-20 11:28:57 | 1302.6 | 0.92 ± 0.03 |
| 3201670141 | 2020-08-20 20:49:25 | 828.0  | 0.83 ± 0.04 |
| 3201670142 | 2020-08-21 04:14:11 | 1722.0 | 1.41 ± 0.03 |
| 3201670142 | 2020-08-21 08:55:29 | 1584.0 | 1.07 ± 0.03 |
| 3201670142 | 2020-08-21 15:04:50 | 1584.0 | 1.46 ± 0.04 |
| 3201670142 | 2020-08-21 20:01:55 | 842.0  | 1.53 ± 0.05 |

Continuation of Table A2

|            |                     |        |             |
|------------|---------------------|--------|-------------|
| 3201670143 | 2020-08-22 00:37:08 | 1372.0 | 0.94 ± 0.03 |
| 3201670143 | 2020-08-22 05:08:36 | 1804.0 | 1.30 ± 0.03 |
| 3201670143 | 2020-08-22 14:25:35 | 858.0  | 1.70 ± 0.05 |
| 3201670144 | 2020-08-22 23:42:54 | 1826.0 | 1.57 ± 0.04 |
| 3201670144 | 2020-08-23 04:14:46 | 1307.0 | 1.56 ± 0.04 |
| 3201670144 | 2020-08-23 08:59:32 | 1408.0 | 1.77 ± 0.04 |
| 3201670144 | 2020-08-23 15:11:55 | 685.0  | 1.45 ± 0.07 |
| 3201670145 | 2020-08-24 03:35:12 | 1426.0 | 1.81 ± 0.04 |
| 3201670145 | 2020-08-24 12:52:09 | 772.0  | 2.35 ± 0.06 |
| 3201670145 | 2020-08-24 17:30:54 | 999.0  | 2.73 ± 0.06 |
| 3201670145 | 2020-08-24 22:10:32 | 1549.1 | 2.37 ± 0.05 |
| 3201670146 | 2020-08-25 02:42:49 | 1517.4 | 2.55 ± 0.05 |
| 3201670146 | 2020-08-25 07:27:32 | 1491.0 | 3.52 ± 0.05 |
| 3201670146 | 2020-08-25 12:06:08 | 1502.0 | 3.35 ± 0.05 |
| 3201670146 | 2020-08-25 16:44:07 | 1460.0 | 2.77 ± 0.05 |
| 3201670146 | 2020-08-25 21:22:49 | 1589.0 | 3.27 ± 0.05 |
| 3201670147 | 2020-08-26 02:01:48 | 1465.0 | 3.77 ± 0.06 |
| 3201670147 | 2020-08-26 06:41:29 | 1638.5 | 3.91 ± 0.05 |
| 3201670147 | 2020-08-26 11:19:46 | 872.0  | 3.70 ± 0.07 |
| 3201670147 | 2020-08-26 14:26:03 | 1481.0 | 3.32 ± 0.05 |
| 3201670147 | 2020-08-26 20:39:25 | 1455.0 | 3.79 ± 0.06 |
| 3201670148 | 2020-08-27 10:38:43 | 1117.0 | 1.94 ± 0.05 |
| 3201670148 | 2020-08-27 15:11:24 | 1747.0 | 1.43 ± 0.04 |
| 3201670148 | 2020-08-27 19:50:26 | 1735.3 | 1.13 ± 0.03 |
| 3201670149 | 2020-08-28 00:46:51 | 679.6  | 1.02 ± 0.05 |
| 3201670149 | 2020-08-28 02:18:03 | 754.4  | 1.61 ± 0.06 |
| 3201670149 | 2020-08-28 11:29:08 | 731.9  | 1.15 ± 0.05 |
| 3201670149 | 2020-08-28 15:57:20 | 260.8  | 1.45 ± 0.10 |
| 3201670149 | 2020-08-28 16:03:23 | 952.6  | 1.35 ± 0.05 |
| 3201670149 | 2020-08-28 20:37:03 | 1231.0 | 1.30 ± 0.04 |
| 3201670150 | 2020-08-29 02:42:46 | 1608.0 | 1.52 ± 0.04 |
| 3201670150 | 2020-08-29 07:22:25 | 1569.0 | 1.91 ± 0.04 |
| 3201670150 | 2020-08-29 13:41:27 | 1096.2 | 1.82 ± 0.05 |
| 3201670150 | 2020-08-29 19:45:21 | 2035.0 | 1.83 ± 0.04 |
| 3201670151 | 2020-08-30 01:56:06 | 1688.0 | 1.86 ± 0.04 |
| 3201670151 | 2020-08-30 09:58:40 | 1004.0 | 1.50 ± 0.05 |
| 3201670151 | 2020-08-30 15:56:11 | 1527.0 | 1.61 ± 0.04 |
| 3201670152 | 2020-08-31 04:15:17 | 1777.0 | 2.36 ± 0.04 |
| 3201670152 | 2020-08-31 10:43:41 | 390.0  | 2.57 ± 0.09 |
| 3201670152 | 2020-08-31 16:39:00 | 901.0  | 2.84 ± 0.06 |
| 3201670152 | 2020-08-31 16:55:57 | 404.0  | 2.23 ± 0.09 |
| 3201670152 | 2020-08-31 22:58:00 | 1069.0 | 3.19 ± 0.06 |
| 3201670153 | 2020-09-01 05:09:58 | 944.0  | 2.96 ± 0.06 |
| 3201670153 | 2020-09-01 11:15:06 | 1317.0 | 2.91 ± 0.06 |
| 3201670154 | 2020-09-01 23:43:31 | 974.0  | 3.28 ± 0.07 |
| 3201670155 | 2020-09-09 15:35:28 | 772.0  | 5.94 ± 0.09 |
| 3201670155 | 2020-09-09 21:47:27 | 953.0  | 5.23 ± 0.08 |
| 3201670156 | 2020-09-10 03:57:28 | 777.0  | 5.64 ± 0.09 |
| 3201670156 | 2020-09-10 10:12:10 | 1149.0 | 5.18 ± 0.07 |
| 3201670156 | 2020-09-10 16:36:04 | 576.0  | 5.47 ± 0.10 |
| 3201670156 | 2020-09-10 22:39:37 | 1023.0 | 5.92 ± 0.08 |
| 3201670157 | 2020-09-11 04:56:23 | 577.0  | 4.98 ± 0.10 |
| 3201670157 | 2020-09-11 10:54:43 | 517.0  | 5.77 ± 0.11 |
| 3201670157 | 2020-09-11 23:18:17 | 983.0  | 5.23 ± 0.07 |
| 3201670158 | 2020-09-12 05:30:23 | 957.0  | 4.67 ± 0.07 |
| 3201670158 | 2020-09-12 11:41:35 | 1025.0 | 3.41 ± 0.06 |
| 3201670158 | 2020-09-12 17:51:33 | 715.0  | 3.82 ± 0.08 |
| 3201670159 | 2020-09-13 06:11:07 | 713.0  | 4.23 ± 0.08 |
| 3201670160 | 2020-09-14 13:28:31 | 869.0  | 3.99 ± 0.07 |
| 3201670160 | 2020-09-14 19:28:45 | 518.0  | 3.65 ± 0.09 |
| 3201670161 | 2020-09-15 01:31:07 | 2153.0 | 3.81 ± 0.04 |

Continuation of Table A2

|            |                     |        |                 |
|------------|---------------------|--------|-----------------|
| 3201670161 | 2020-09-15 07:43:54 | 856.0  | $3.53 \pm 0.07$ |
| 3201670161 | 2020-09-15 20:10:18 | 515.0  | $3.06 \pm 0.08$ |
| 3201670162 | 2020-09-16 08:36:46 | 532.0  | $3.48 \pm 0.09$ |
| 3201670162 | 2020-09-16 14:50:07 | 1576.0 | $2.92 \pm 0.05$ |
| 3201670162 | 2020-09-16 21:05:09 | 934.0  | $2.77 \pm 0.06$ |
| 3201670167 | 2020-09-21 04:44:27 | 271.0  | $0.81 \pm 0.07$ |
| 3201670167 | 2020-09-21 17:06:48 | 1013.0 | $1.44 \pm 0.05$ |
| 3201670168 | 2020-09-22 11:51:05 | 1098.0 | $1.95 \pm 0.05$ |
| 3201670168 | 2020-09-22 17:51:57 | 856.0  | $2.52 \pm 0.06$ |
| 3201670169 | 2020-09-23 04:48:04 | 1333.0 | $0.92 \pm 0.03$ |
| 3201670169 | 2020-09-23 06:20:43 | 1440.0 | $1.53 \pm 0.04$ |
| 3201670170 | 2020-09-24 03:47:48 | 2315.0 | $2.18 \pm 0.04$ |
| 3201670170 | 2020-09-24 17:51:47 | 1876.0 | $1.08 \pm 0.03$ |
| 3201670171 | 2020-09-25 00:08:10 | 427.0  | $1.54 \pm 0.07$ |
| 3201670171 | 2020-09-25 20:04:12 | 1103.0 | $1.57 \pm 0.05$ |
| 3201670172 | 2020-09-26 08:27:44 | 1140.0 | $0.74 \pm 0.04$ |
| 3201670172 | 2020-09-26 21:09:11 | 1249.0 | $1.80 \pm 0.05$ |
| 3201670174 | 2020-09-28 14:45:24 | 1024.0 | $2.64 \pm 0.06$ |
| 3201670175 | 2020-09-29 03:03:50 | 2083.0 | $1.32 \pm 0.03$ |
| 3201670175 | 2020-09-29 15:33:30 | 2154.0 | $1.28 \pm 0.03$ |
| 3201670176 | 2020-09-30 22:31:45 | 334.0  | $0.80 \pm 0.07$ |
| 3201670177 | 2020-10-01 10:55:46 | 1453.0 | $1.01 \pm 0.04$ |
| 3201670177 | 2020-10-01 17:01:30 | 1599.0 | $0.93 \pm 0.03$ |
| 3201670179 | 2020-10-03 06:37:27 | 354.4  | $0.71 \pm 0.06$ |
| 3201670180 | 2020-10-04 13:19:08 | 303.9  | $1.23 \pm 0.08$ |
| 3201670184 | 2020-10-08 02:45:23 | 1117.0 | $1.11 \pm 0.04$ |

End of Table

This paper has been typeset from a  $\text{\TeX}/\text{\LaTeX}$  file prepared by the author.

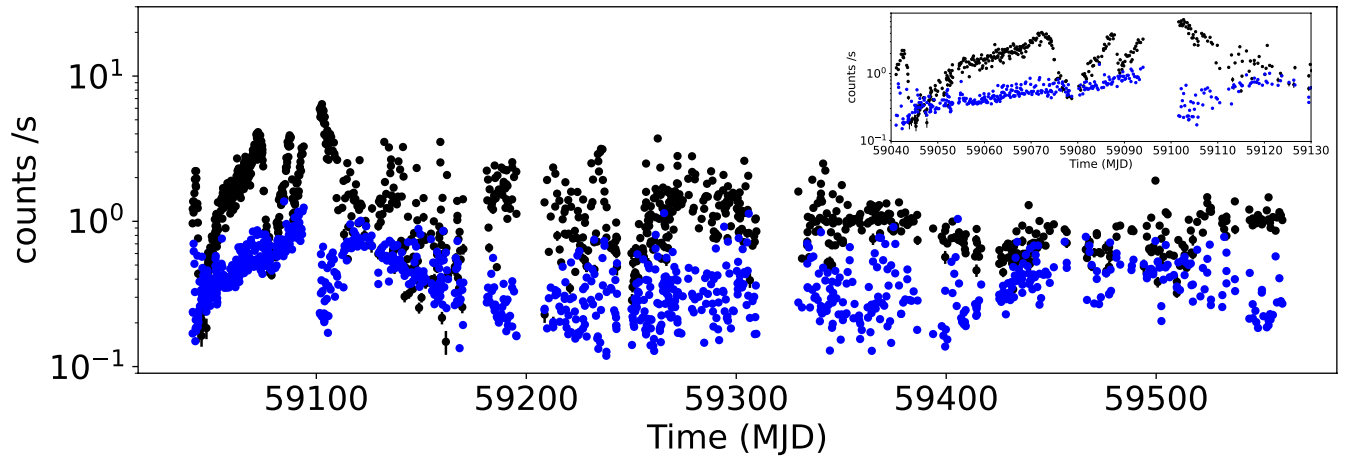


**Figure A1.** The *NICER* light curve of the 0.3-1.1 keV band (black) and the background light curve of the 0.3-1.1 keV band (blue). The insert shows the zoomed-in view of the early flares (MJD < 59130).



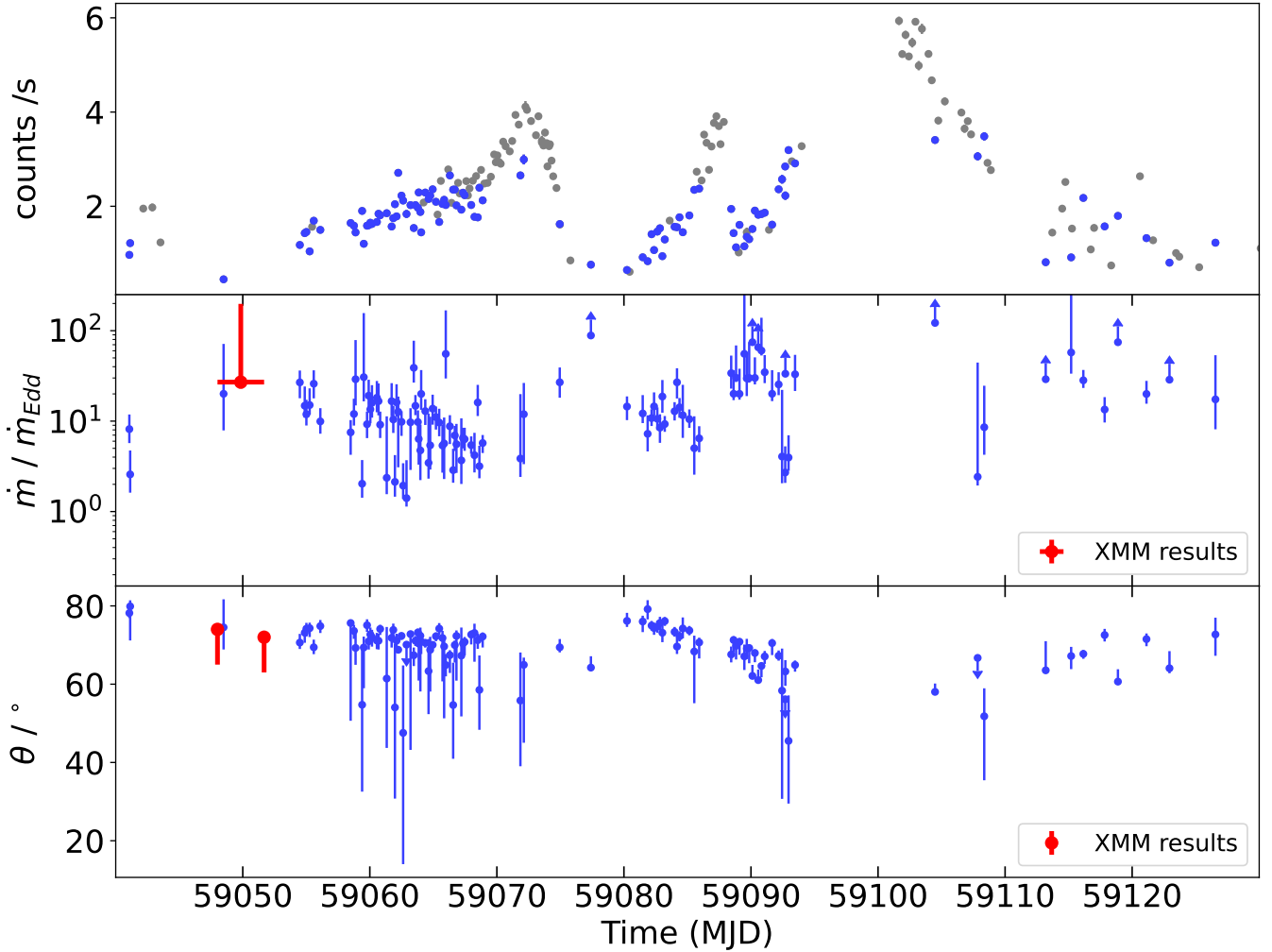


**Figure A2.** *Top panel:* The *NICER* 0.3–1.1 keV early–time source light curve. We only consider the epochs where the source flux stays above the background level from 0.3 keV to at least 0.6 keV (a total of 206 epochs in the early period). Spectra in epochs marked by blue dots are well–fit ( $C\text{-stat}/d.o.f. < 2$ ; 108 in total) by the model in this analysis, while grey dots mark spectra that have  $C\text{-stat}/d.o.f. > 2$ . The fit–function here is different from Fig. 6:  $\text{TBabs}*\text{s1imdz}$ . *Middle panel:* Constraints on the disc mass accretion rate  $\dot{m}$  derived from the *NICER* spectra obtained before MJD 59130. We fit each of the 206 spectra individually allowing the accretion rate  $\dot{m}$  and the inclination  $\theta$  to vary. We use  $N_H = 1 \times 10^{20} \text{ cm}^{-2}$  for all spectral fits in this paper. We fix  $M_\bullet = 7 \times 10^5 M_\odot$  and  $a_\bullet = 0.9$  based on the results of the spectral fits to the *XMM-Newton* data (Fig. 5). We show the fitted parameter values for the 108 out of the 206 spectra where the  $C\text{-stat}/d.o.f. < 2$  (the results from the blue points in the top panel). The accretion rate constrained from the joint–fit to the XMM#1 and XMM#2 X–ray spectra is marked with the red dots. *Bottom panel:* Constraints on the inclination  $\theta$  derived from the same fitting procedure described above. We conclude that the slim disc alone cannot explain the early–time *NICER* data well, especially the hard spectra at the peak of the flares are not well fit.

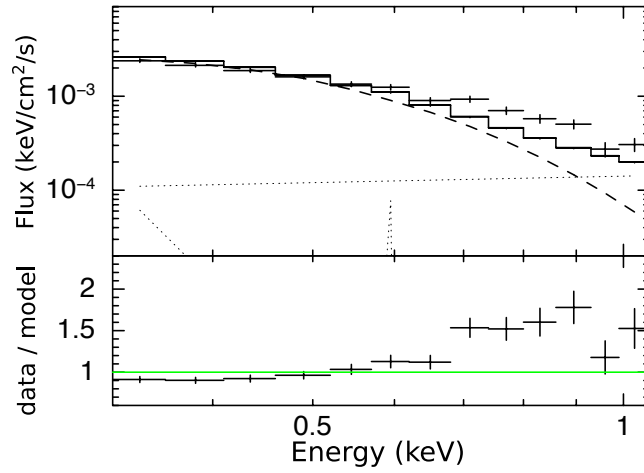


**Figure A3.** Top panel: An example of the hard *NICER* spectra at flare peaks, taken on MJD 59074.4. The fit-function is comprised of the following model components:  $\text{TBabs}*\text{slimdz}$ . The fit procedure is described in Section 3.3.2 and Fig. A2. The solid, dashed, and dotted lines represent the total model, the slim disc emission, and the contribution from the background as determined from fitting the estimated background-only spectrum separately, respectively. The best-fit background power-law indices and Gaussian parameters have been held constant during the fit to the source+background spectra. Bottom panel: We show the ratio between the observed number of counts (data) and the predicted number of counts in each bin (model). The spectra at flare peaks are much harder than a continuum described by a slim disc.

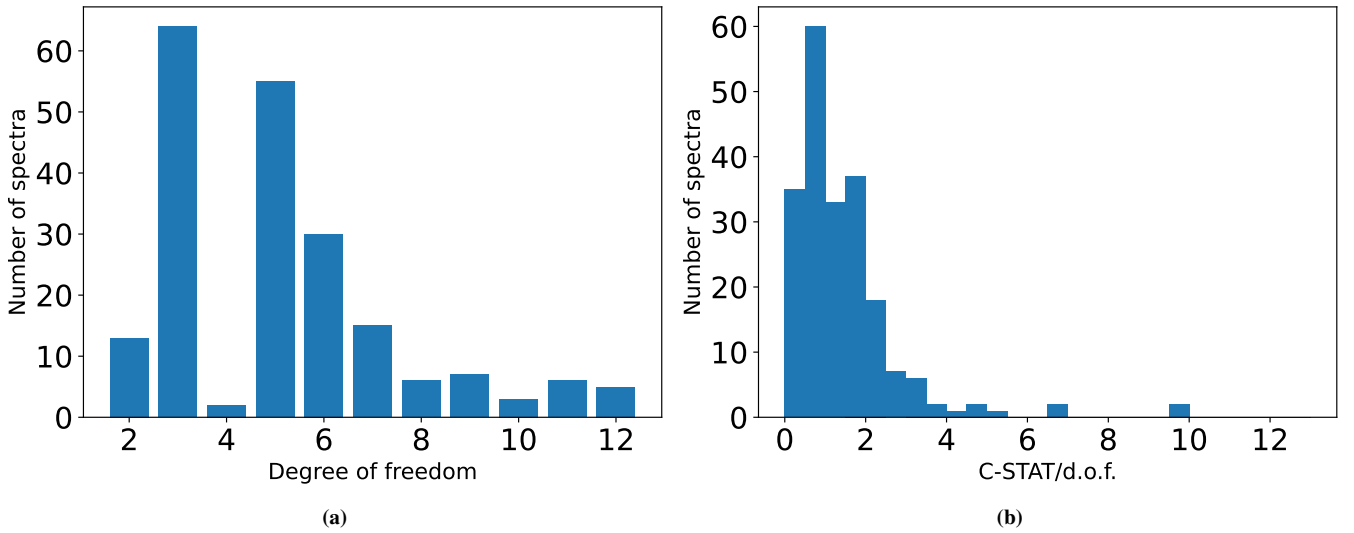


**Figure A4.** *Left:* Histogram of the degree-of-freedom (d.o.f) in each fit produced by the fit procedure described in Section 3.3.2 and of which the results are shown in Fig. 6. Each spectrum has at least 2 d.o.f. left to be fitted with the 2-parameter ( $\theta$  and  $kT_e$ ) fit function. *Right:* Histogram of the C-stat/d.o.f. produced by the same fit procedure.

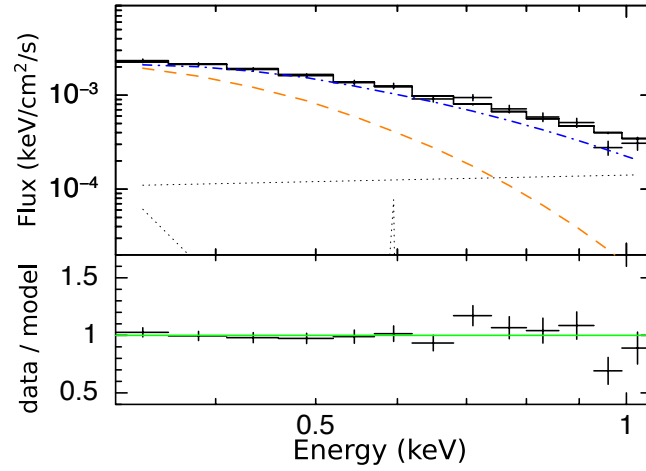


**Figure A5.** Same as Fig A3 but with a fit-function comprising of the following model components: `TBabs*thcomp*slimdz`. Moreover, the orange dashed line represents the slim disc emission before the inverse-Comptonisation, and the blue dash-dotted line represents the slim disc emission after the inverse-Comptonisation. The C-stat/d.o.f. = 13.9/11.

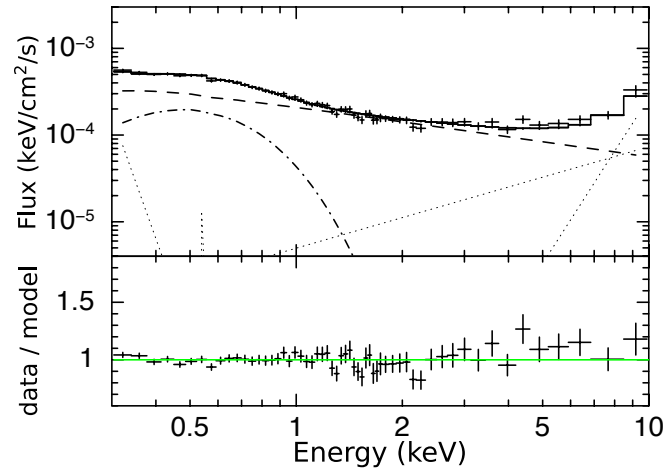


**Figure A6.** Top panel: phenomenologically fitting the XMM#3 spectrum with a fit function comprised of a power-law and a black body. In XSPEC's syntax, the fit function is `"TBabs*(powerlaw+zbody)"`. The solid, dashed, dot-dashed, and dot lines represent the best-fit total model, the power-law, the black body emission, and the contribution from the background as determined from fitting extracted spectra from background-only data separately, respectively. Bottom panel: The ratio between the observed number of counts (data) and the best-fit predicted number of counts in each spectral bin (model).

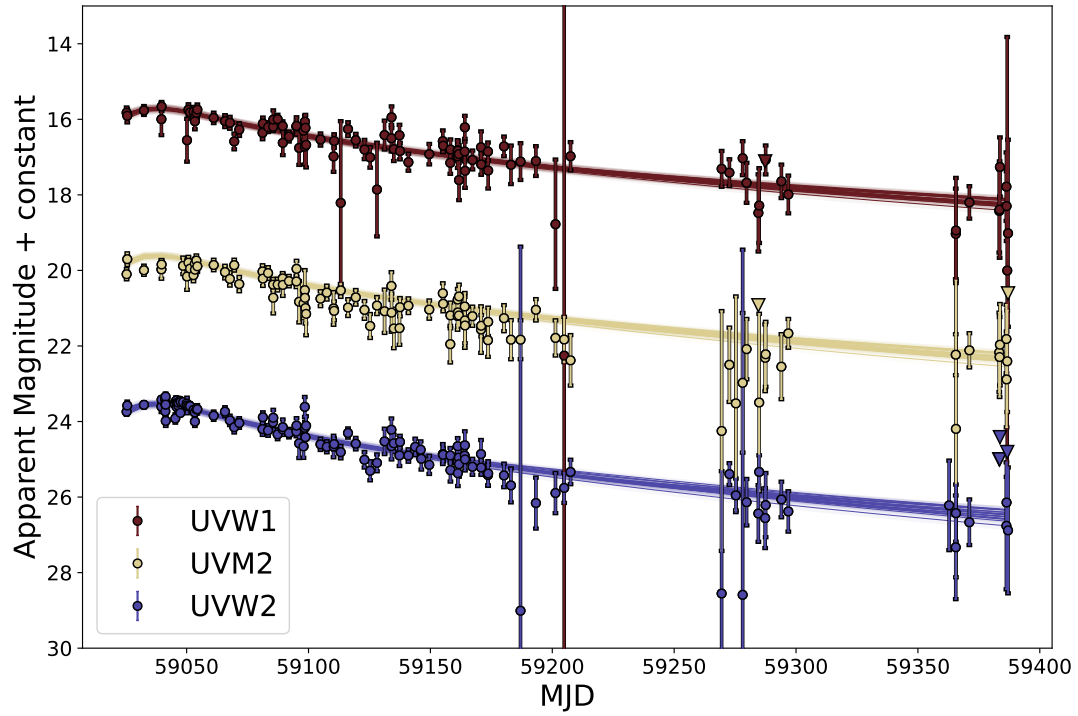
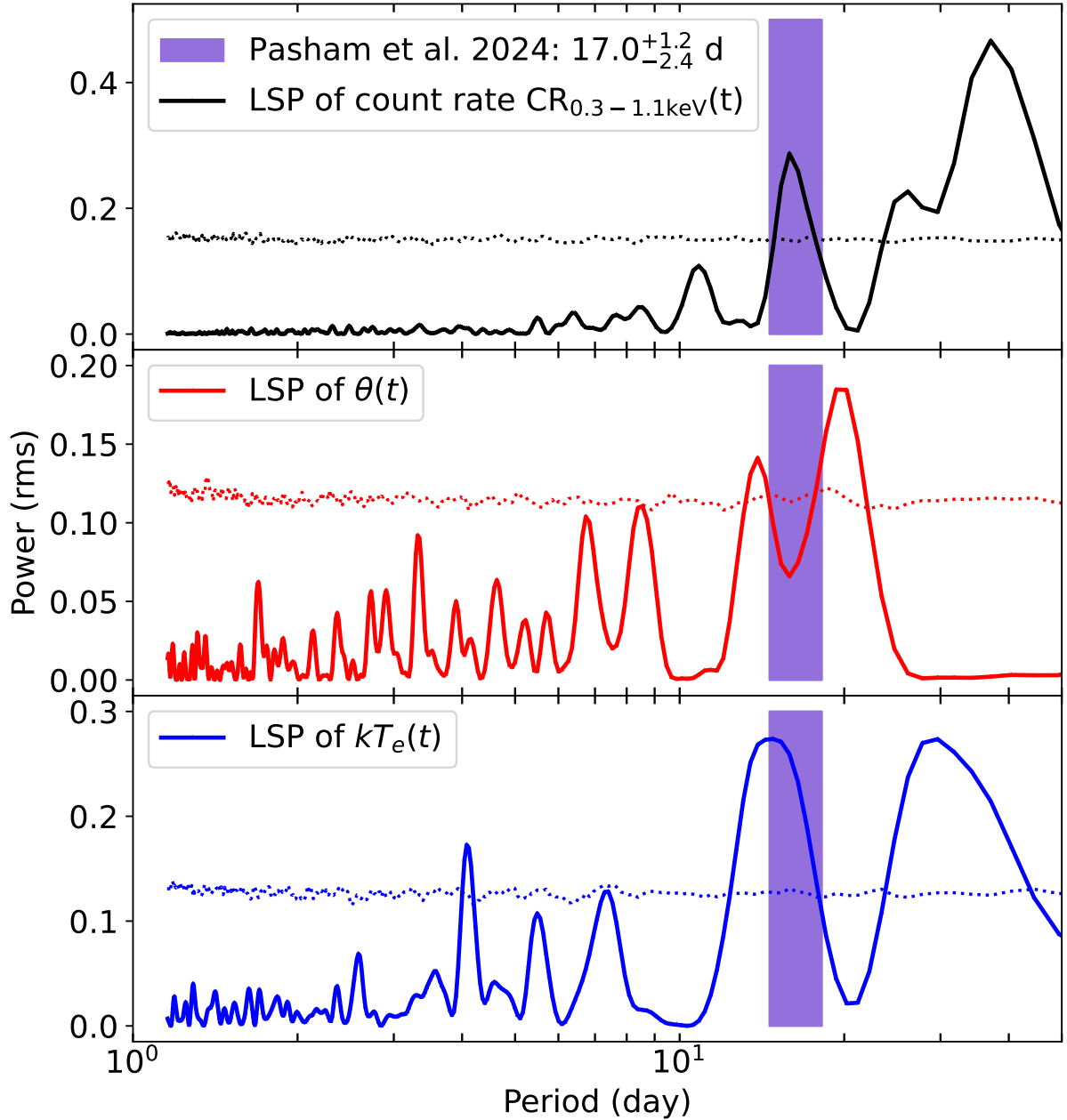


**Figure A7.** *Swift*/UVOT data fitted using the MOSFiT, as described in Section 3.4. We shift the y-axis of UVW1 and UVW2 bands by a constant (-4 for UVW1 and +4 for UVW2) for plot clarity.



(a)

**Figure A8.** Lomb–Scargle periodograms (LSPs) calculated from the X–ray count rate (CR) in 0.3–1.1 keV (*solid black*), the measured inclination  $\theta$  (*solid red*) and electron temperature  $kT_e$  (*solid blue*), from the results in Fig. 6. The x–axis is the period, and the y–axis is the LSP power for a given periodic mode. All three parameters are derived or measured over the period MJD 59041–59130. Dotted lines are the  $3\sigma$  detection thresholds, which is roughly estimated by a bootstrapping approach similar to that in [Evans et al. 2023](#): for each time series (the count rate,  $\theta$ , or  $kT_e$ ), we redistribute the value of the parameter under consideration randomly among the same set of time bins as the original, simulating a new time series. We perform 10000 such simulations and then calculate the Lomb–Scargle periodogram of each simulation. The 99.7 percentile of power at each frequency is then calculated. We note a better treatment of the significance estimation should include modelling the red noise in the lightcurves, which is beyond the purpose of this paper and can be found in [Pasham et al. 2024](#). The periodicity peaks in the count rate and  $kT_e$  are consistent with a period of  $17^{+1.2}_{-2.4}$  days (*purple*) found by [Pasham et al. 2024](#), while the LSP of  $\theta$  only shows two weak peaks around 17 days. As the IC component dominates the spectrum during the flares, it is possible that most of the periodicity is imprinted in the IC component, while the periodicity in  $\theta$  is less observed. A double–period peak can be found in the LSPs of the count rate, and the  $kT_e$ . Meanwhile, the LSP of  $kT_e$  also shows a 4–day peak that barely reaches the  $3\sigma$  level, which corresponds to no signals in the data (the LSP of the 0.3–1.1 keV count rate lightcurve) and is likely a noise component.

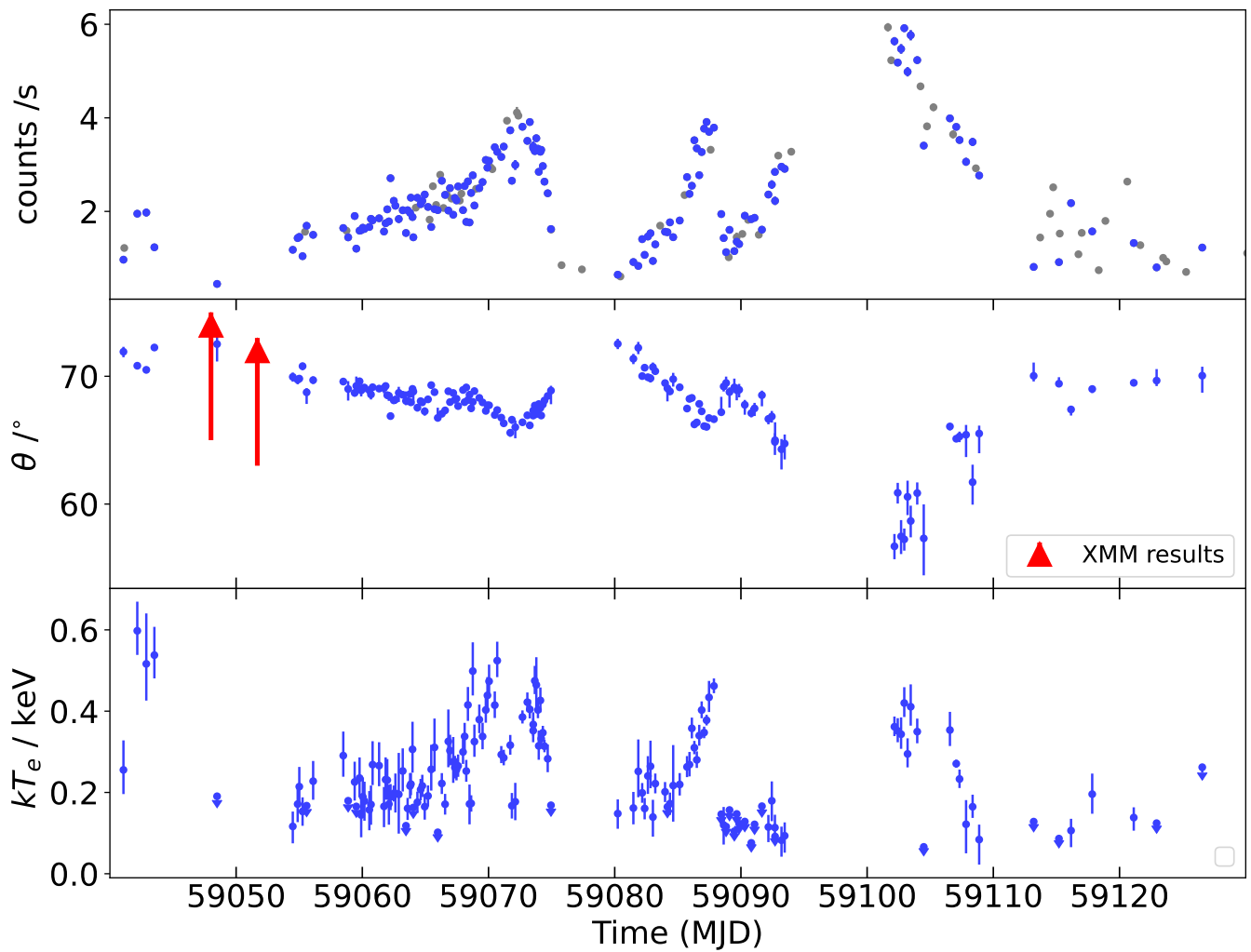


**Figure A9.** Same as Fig. 6, but in deriving these panels, we fixed the covering fraction of the IC component to 0.5 instead of unity when fitting the *NICER* spectra. In total, 152 out of 206 spectra are fitted with  $C\text{-stat}/d.o.f. < 2$  (blue data points).

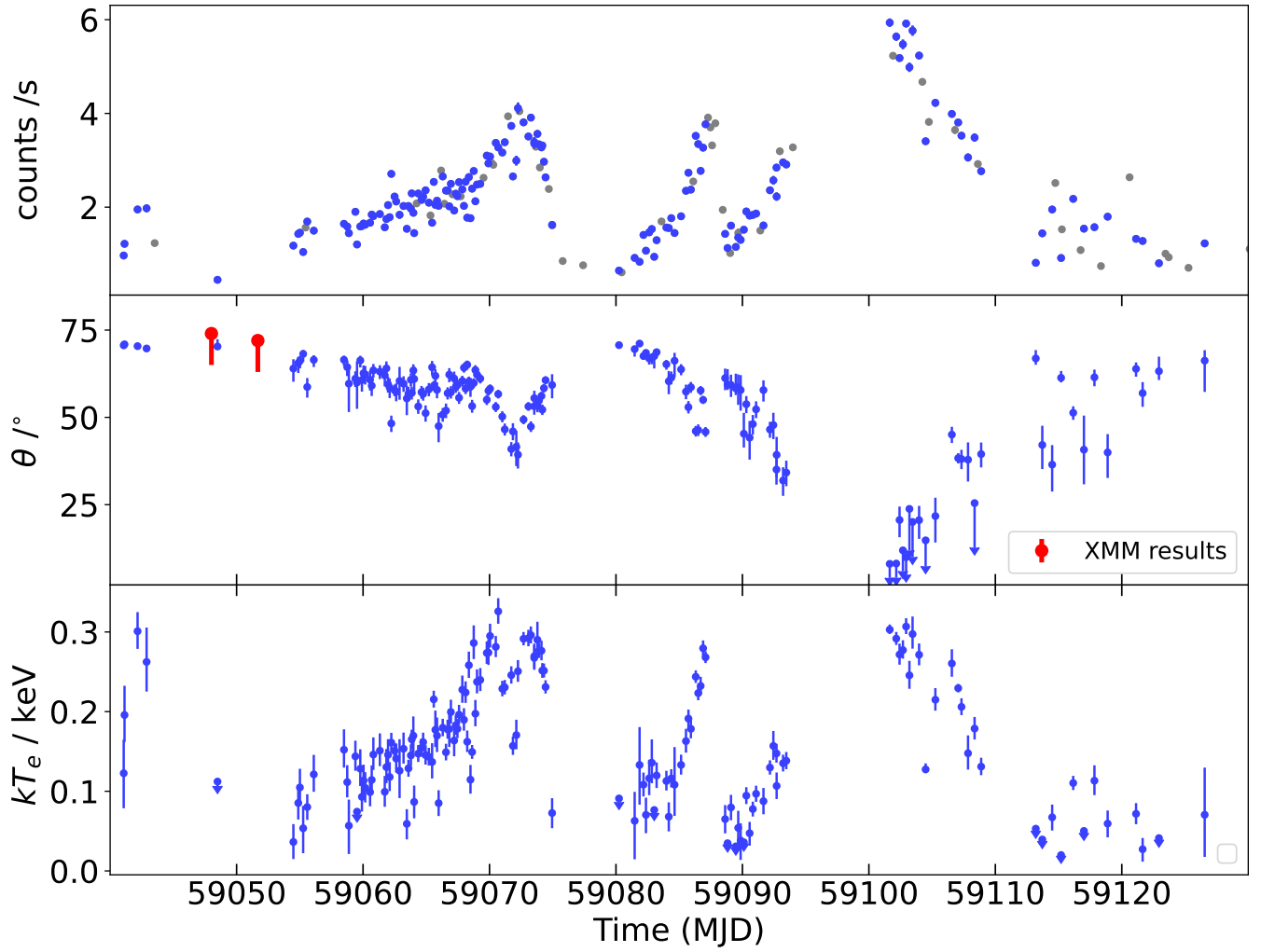


**Figure A10.** Same as Fig. 6, but we fix  $M_\bullet$  to  $5 \times 10^5 M_\odot$  and  $a_\bullet$  to 0.2 when fitting the *NICER* spectra. In total, 160 out of 206 spectra are fitted with  $C\text{-stat}/d.o.f. < 2$ .

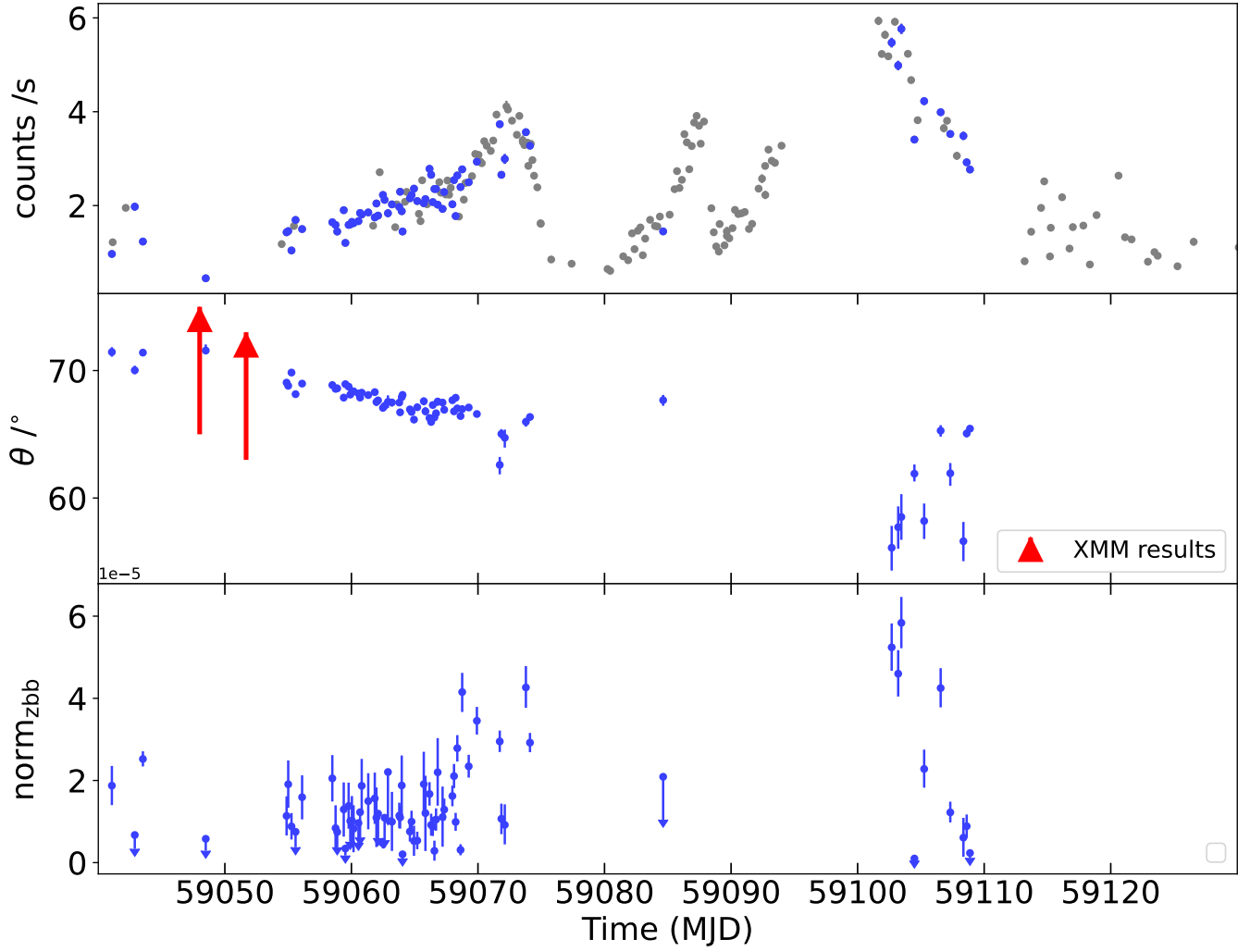


**Figure A11.** Same as Fig. 6, but to derive these panels we used a fit-function of  $\text{TBabs}*(\text{sllimdz}+\text{zbody})$  when fitting the *NICER* spectra. The black body temperature is fixed to 0.3 keV during the fit. In total, 71 out of 206 spectra are fitted with  $C\text{-stat}/\text{d.o.f.} < 2$  (blue data points in the *top* panel). Allowing the black body temperature to be free-to-vary during the fit would increase the number of good-fits to 115 out of 206 but still far less than Fig. 6 (165 out of 206).



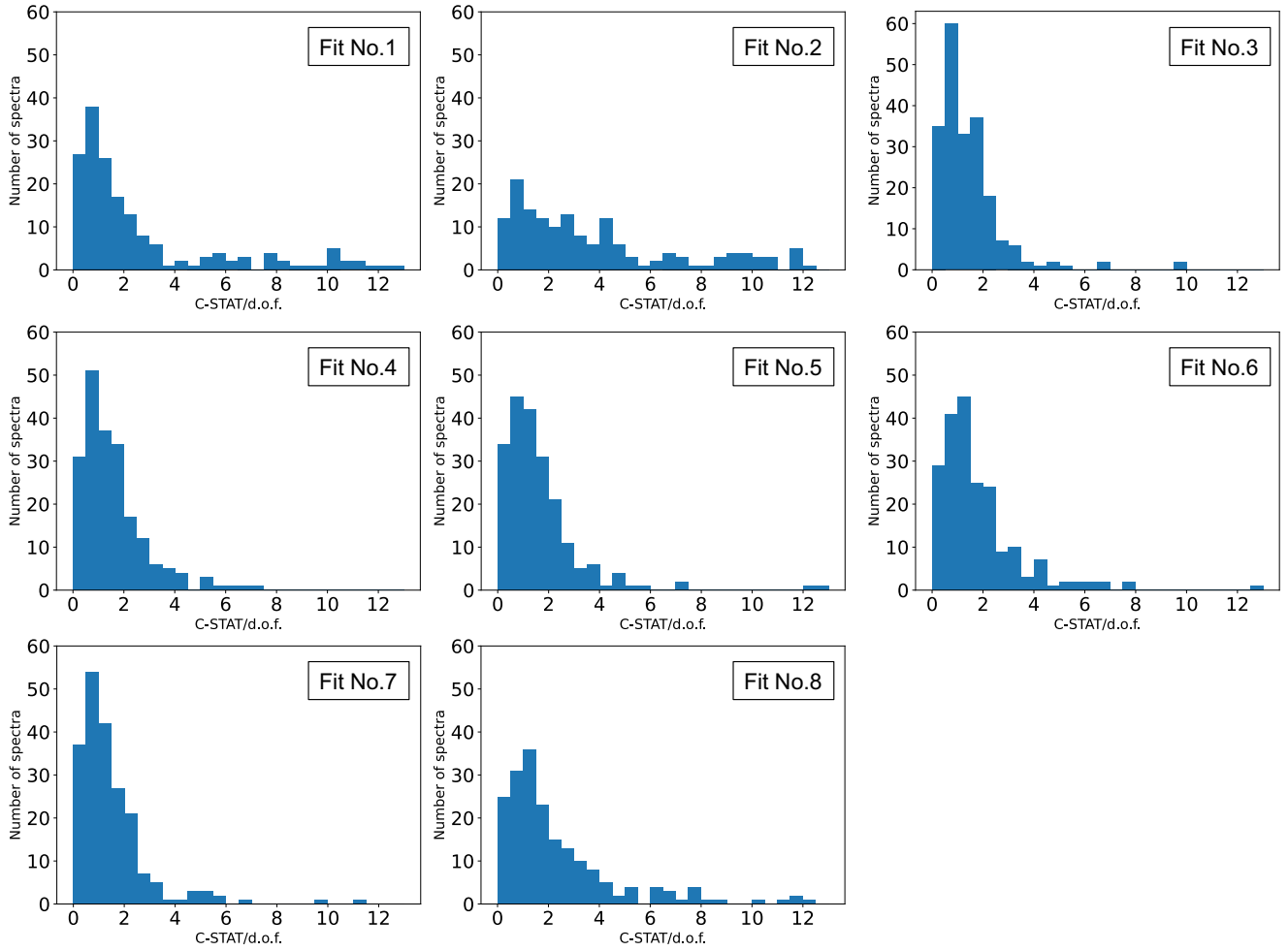


**Figure A12.** Histograms of the C-stat/d.o.f. produced by the fits performed in this paper. Labels show from which fit each histogram is derived, and details of each fit are listed in Table 5. The third figure is identical to Fig. A4b, and other histograms are comparable to it.